Accepted Manuscript

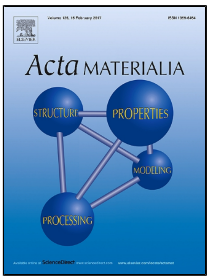

Room temperature ferromagnetism and ferroelectricity in strained multiferroic $BiFeO_3$ thin films on $La_{0.7}Sr_{0.3}MnO_3/SiO_2/Si$ substrates

M.C. Ramírez-Camacho, C.F. Sánchez-Valdés, J.J. Gervacio-Arciniega, R. Font, C. Ostos, D. Bueno-Baques, M. Curiel, J.L. Sánchez-Llamazares, J.M. Siqueiros, O. Raymond-Herrera

PII:	S1359-6454(17)30121-0
DOI:	10.1016/j.actamat.2017.02.030
Reference:	AM 13558
To appear in:	*Acta Materialia*
Received Date:	29 September 2016
Revised Date:	07 February 2017
Accepted Date:	09 February 2017

Please cite this article as: M.C. Ramírez-Camacho, C.F. Sánchez-Valdés, J.J. Gervacio-Arciniega, R. Font, C. Ostos, D. Bueno-Baques, M. Curiel, J.L. Sánchez-Llamazares, J.M. Siqueiros, O. Raymond-Herrera, Room temperature ferromagnetism and ferroelectricity in strained multiferroic $BiFeO_3$ thin films on $La_{0.7}Sr_{0.3}MnO_3/SiO_2/Si$ substrates, *Acta Materialia* (2017), doi: 10.1016/j.actamat.2017.02.030

Room temperature ferromagnetism and ferroelectricity in strained multiferroic $BiFeO_3$ thin films on $La_{0.7}Sr_{0.3}MnO_3/SiO_2/Si$ substrates

M. C. Ramírez-Camacho[1,2], C. F. Sánchez-Valdés[2], J. J. Gervacio-Arciniega[2], R. Font[3], C. Ostos[4], D. Bueno-Baques[5], M. Curiel[6], J. L. Sánchez-Llamazares[7], J. M. Siqueiros[2], O. Raymond-Herrera[2]

[1]Posgrado en Física de Materiales, Centro de Investigación Científica y de Educación Superior de Ensenada, Carretera Tijuana-Ensenada 3918, Zona Playitas, 22860 Ensenada, B. C., México.

[2]Centro de Nanociencias y Nanotecnología, Universidad Nacional Autónoma de México, AP 14, Ensenada 22860, Baja California, México

[3]Facultad de Física, Universidad de La Habana, San Lázaro y L, 10400 La Habana, Cuba

[4]Instituto de Química, Universidad de Antioquia, UdeA, Calle 70 No. 52-21, Medellín, Colombia

[5] Center for Advanced Technologies and Optical Materials, Dept. of Physics and Energy Science, University of Colorado, Colorado Springs, Colorado 80918, USA.

[6]Instituto de Ingeniería, Universidad Autónoma de Baja California, Mexicali 21280, Baja California, México

[7]Instituto Potosino de Investigación Científica y Tecnológica A.C., Camino a la Presa San José 2055, Col. Lomas 4ª, San Luis Potosí 78216, México.

ABSTRACT

A novel ferromagnetic state coexisting with ferroelectric ordering at room temperature in strained $BiFeO_3$ (BFO) thin films grown using a sputtering technique on $La_{0.7}Sr_{0.3}MnO_3/SiO_2/Si(100)$ (LSMO/SOS) substrates is reported. The properties of BFO films with different thicknesses (t_{BFO} = 15, 50, 70, 120, and 140 nm) on 40 nm LSMO layers are explored. [012] *out-of-plane* highly textured BFO/LSMO stacks grew with rhombohedral structures. LSMO layers are nanostructured in nature, constituted by ferromagnetic single-

domain nanoregions induced by the constrain of the SiO_2 surface, with $T_C \sim 200$ K and high coercive field (H_C) of ~ 1100 Oe at 2.5 K. BFO films grew epitaxially nanostructured on LSMO, exhibiting ~ 4 nm spherical nanoregions. The BFO layers show typical antiferromagnetic behavior (in a greater volume fraction) when made thicker ($t_{BFO} > 70$ nm). The thinner films ($t_{BFO} < 50$ nm) display ferromagnetic behavior with $T_C > 400$ K, $H_C \sim 1600$ Oe for 15 nm and ~1830 Oe for 50 nm. We propose that such ferromagnetic behavior is originated by the establishment of a new magnetic configuration in the Fe^{3+}-O-Fe^{3+} sublattice of the BFO structure, induced by strong hybridization at the interface as consequence of superexchange coupling interactions with the ferromagnetic Mn^{3+}-O-Mn^{3+}/Mn^{4+} sublattice of LSMO. All BFO layers show excellent ferroelectric and piezoelectric properties (coercive field ~ 740 kV/cm, and d_{33} = 23 pm/V for 50 nm; ~ 200 kV/cm and 55 pm/V for 140 nm), exhibiting 180º and 109º DWs structures depending on the thickness. Such multiferroic properties predict the potential realization of new magneto-electronic devices integrated with Si technology.

KEYWORDS: *multiferroic, BFO/LSMO thin film, rf sputtering, interlayer exchange coupling, superexchange*

1. INTRODUCTION

Single-phase or composite multiferroic (MF) materials, characterized by the coexistence of two or more ferroic orders (ferroelectric (FE), ferromagnetic (FM), ferroelastic, among others), have generated significant interest due to the possible additional functionality provided by the coupling between the different ferroic orders. In particular, special attention have been devoted to study of materials showing a magnetoelectric (ME) coupling (FE-FM) which has the potential to enable the control of electric polarization by a magnetic field and the control of magnetization by an electric field [1-8]. Among ME materials, a significant effort has been dedicated to artificially engineered materials that combine FE and FM constituents in materials with two- or more-phases in horizontal and/or vertical architectures [1, 4, 7, 9, 10]. In these compounds, the interplay between magnetic and electric ordering, and transport properties, reveals new physics that could be used to design novel functional devices based on FE/MF tunnel junctions, resistance switching, photovoltaic effect, tunable giant magnetoresistance spin valves, etc [1-10]. Such materials combinations enable the

development of a new family of electronic devices such as ultrahigh-density magnetic memories, ultralow-power tunable radio-frequency/microwave ME devices, low magnetic field sensors, to name a few [4, 7].

Today, the ability to create atomically perfect, lattice-matched heterostructures of complex perovskite oxides using thin film growth techniques as molecular beam epitaxy (MBE), pulsed laser deposition (PLD), and atomic layer deposition (ALD), has generated new physical phenomena at interfaces where exotic properties and unexpected states are originated from the lattice, charge, orbital, and spin coupling [1,2,6, 11,12]. In the last years, many detailed studies on MF epitaxial interfaces have been reported where strong coupling effects such as exchange bias, electronic orbital reconstruction, orbital switching, exchange-spring magnet, and interdiffusion processes phenomena occur [1-3, 6, 11-18].

Among the single-phase MF compounds, many complex oxides families have been extensively investigated, especially those with perovskites or perovskite-like structure such as the rare-earth manganates and the well-known Bi-based materials [1-2]. However, most of those reported multiferroics so far are antiferromagnetic (AFM) with Curie or Néel temperatures far below room temperature (RT). In this field, the AFM-FE $BiFeO_3$ (BFO) compound with Curie temperature of ~ 1090 K and Néel temperature of ~ 640 K is, perhaps, the most investigated MF material from the experimental and theoretical points of view, appealing for RT applications [1-21]. Nevertheless, taking in to account its AFM behavior many efforts have been focused on the control of the FE domain structure, the domain switching mechanisms and the ME coupling through the extrinsic exchange coupling between its MF ordering and other FM, FE, or MF compounds in epitaxial heterostructures or nanocomposites where the above mentioned interface phenomena arise [1-22]. In particular, one of the FM materials used to investigate and understand the interfacial coupling is the well-known half-metallic ferromagnet $La_{0.7}Sr_{0.3}MnO_3$ (LSMO) which exhibits fascinating physical properties such as a high Curie temperature ~ 370 K, colossal magnetoresistance at RT, magnetic anisotropy, and a measured spin polarization of nearly 100% [22, 23] with high potential for applications in spintronics and novel functional electronic devices [4,7,19,20]. Under this premise, the BFO/LSMO bilayers grown on different substrates have been widely investigated in the academic world. On the other hand, due to incompatibility of the monocrystalline oxide substrates (SrTiO3 (STO), $LaAlO_3$,

$DyScO_3$, and $NdGaO_3$) used to date with the actual Si-based technology, some works have been directed to explore silicon integrated multiferroic heterostructures as in recent studies in epitaxial BFO/LSMO stacks grown on traditional Si substrates, buffered with STO/MgO/TiN stacks [17, 19, 20].

Motivated by the physical phenomena arising at the multiferroic heterostructures interfaces and to explore different deposition techniques compatibles with Si technology, the aim of this work is the study of the multiferroic properties of BFO/LSMO thin films grown on SiO2/Si(100) substrates using rf-sputtering, with different nanoscale thicknesses of the BFO layer. A detailed study of the structural, magnetic and ferroelectric properties is presented. A novel nanostructured ferromagnetic phase coexisting with the ferroelectric order at RT for the BFO films with thickness smaller than 50 nm was found. A model based on strong superexchange coupling interactions arising at the interface between the strained Fe^{3+}-O-Fe^{3+} sublattice of BFO with the ferromagnetic Mn^{3+}-O-Mn^{3+}/Mn^{4+} sublattice of LSMO is discussed.

2. EXPERIMENTAL DETAILS

Multiferroic BFO/LSMO bilayers were deposited on SiO_2/Si(100) (SOS) commercial substrate using the rf-magnetron sputtering technique. Stoichiometric LSMO and BFO ceramic targets were fabricated by typical solid state reaction. LSMO thin films with 40 nm thickness were directly grown on SOS. The LSMO/SOS stack is labeled L40 across the paper. All films thicknesses were obtained using transmission electron microscopy (TEM). The deposition parameters for LSMO films were: 2.0×10^{-5} Torr base pressure, 5 cm target–substrate distance, 500 °C substrate temperature, 250 W rf-power, partial pressures of Ar (15 mTorr) and O (5 mTorr) totaling 20 mTorr, and 15 min deposition time. For the BFO film deposition process, the parameters used were: 400 °C substrate temperature, 150 W rf-power, partial pressures of Ar (20 mTorr) and O (5 mTorr) totaling 25 mTorr, and deposition times of 5, 10, 15, 20, and 30 min leading to BFO film thickness (t_{BFO}) values of 15, 50, 70, 120, and 140 nm, respectively. The labeling convention for the BFO/LSMO/SOS stacks studied in this work is, according to the BFO films thickness, B15, B50, B70, B120 and B140, respectively.

The structural and chemical compositions characterization was realized by X-ray diffraction

(XRD) using a PanAnalytical X-Pert PRO MRD diffractometer with monochromatic Cu Kα_1 radiation (1.540598 Å) and by scanning transmission electron microscopy (STEM) with energy dispersive spectroscopy (STEM+EDS) using a JEOL JEM-2100F and a JEOL JEM2200FS microscopes with 200 kV accelerating voltage. Cross-sectional specimens were prepared using a JEOL JIB-4500 scanning electron microscope equipped with focused ion beam technique (SEM+FIB). All the specimens were first coated with Au at room temperature using argon-ion sputtering technique to protect the film´s surface from Ga beam damage. Structural simulation was carried out using the *Diamond* software (version 3.2k) [24].

The magnetic characterization was performed using a Physical Properties Measurement System equipped with a vibrating sample magnetometer option from Quantum Design (9 T Dynacool® platform). All samples were prepared rectangular in shape with similar dimensions (in lengths and area). The magnetic field was *in-plane* applied, along the larger dimension, to minimize the demagnetization field effect. The temperature-dependence magnetization curves $M(T)$ in zero-field-cooling (ZFC) and field-cooling (FC) modes were measured at low magnetic field H = 200 Oe, between 2.5 K and 400 K, with a heating and cooling ramp of 1 K/min. The $M(T)$ curves under high magnetic field (50 kOe) were only performed in FC from 400 K to 2.5 K using the same cooling rate. The hysteresis loops were recorded at a maximum magnetic field of ± 40 kOe at selected temperatures from 2.5 K to 400 K, using a magnetic field sweep rate of 100 Oe/s. All magnetization values reported here were normalized to the total volume of the LSMO single layer or of the BFO/LSMO bilayers, using the thickness and area values pertinent to the individual case. Moreover, the diamagnetic contribution of the SiO2/Si substrate was subtracted for all samples.

Surface topography, *out-of-plane* FE domain structure, domain switching, and FE hysteresis behavior were studied by piezoresponse force microscopy (PFM) using an XE-70 (Park Systems) equipped with an SR865 lock-in amplifier (Stanford Research Systems), using Multi75-G probes with chrome-platinum conductive coating (Budget Sensors). An AC voltage signal of 1 V_{pp}, at a frequency value near the contact resonance of 342.5 kHz was used. The LSMO film was used as bottom electrode. All PFM characterizations were carried out at 9 % humidity and 21 ºC.

3. RESULTS AND DISCUSSION

3.1. Structural characterization

The collected XRD data of the BFO/LSMO/SOS and LSMO/SOS stacks are shown in Figure 1a, where intensities are illustrated in logarithm scale. To properly assess the evolution of the phases, present in each sample, the peak at $2\theta = 69.05°$ for L40 sample corresponding to the (400) reflection of the Si substrate is used as internal standard; hence, each pattern was realigned accordingly. The XRD pattern of the as-deposited LSMO single layer shows a strong *out-of-plane* preferential growth with the orientation (012). The peaks at 22.58° and 46.23° (labeled with the * symbol), are in good correspondence with the rhombohedral structure ($R\bar{3}c$ space group, SG 167) reported for LSMO with the obtained hexagonal lattice parameters a_{LSMO} = 5.529 Å and c_{LSMO} = 13.700 Å (see Fig. 2a). These are larger than those reported by Hibble *et al* in the ICSD 88409 card of a = 5.5085 Å and c = 13.3717 Å at room temperature [25]. As can be seen from structural simulation presented in Fig. 2 (generated using the *Diamond* software [24] and based on the XRD data), the (012) and (024) planes in the LSMO structure (Fig. 2a) are described by crossed Mn-O-Mn and La/Sr-O-La/Sr chains, respectively, where the Mn^{3+}/Mn^{4+} ions occupying the octahedral *B* site are six-fold coordinated while the La^{3+}/Sr^{4+} ions occupying the *A* site are nine-fold coordinated. A such highly textured (012) growth of the LSMO film and the increase on the lattice parameters could be a result of the local incommensurate coupling of the crossed Mn-O-Mn chains arrangement (conforming four-membered rings, and characterized by Mn-O bond length of 1.94 Å, O-Mn-O angles of 89.96º and 90.04º, and Mn-O-Mn angle of 166.50º) with the Si-O-Si two-dimensional array at the surface of the native amorphous ultrathin SiO_2 (SO) film (~ 6 nm thickness, see Fig. 3a) on the Si wafers. Thus, the Mn-O-Mn arrangement is constrained by the local ordering parameters of the Si-O-Si surface characterized by a Si-O bond length of 1.61 Å, O-Si-O angle of ~ 110º, and Si-O-Si angle of 160º according to previous studies using reactive molecular dynamics [26, 27] and where the planar rings with lowest energy of formation are four-membered rings [27]. Moreover, the bright field cross-section TEM image in Fig. 3a shows a relaxed LSMO thin film with the (012) preferential orientation (where the measured interplanar distance of 3.86 Å is in good agreement with the obtained a_{LSMO} and c_{LSMO} parameters) and a continuous LSMO/SO interlayer connection

(without appreciable grain boundaries) is observed with an interface thickness of ~ 4 nm. This last feature, establishes a distinction within the sharp grain boundaries observed in the compressive strained 50 nm LSMO thin film grown by molecular beam epitaxy (MBE) on epitaxial $CaTiO_3$-buffered silicon substrates and the formation of a 10 nm amorphous SiO_x layer reported by Adamo *et al* [28]. On the other hand, the low intensity peak at $2\theta \sim 32.36°$ corresponding to the $(\bar{1}20)$ and $(\bar{1}14)$ planes, reveals the *in-plane* misorientation, and all together with the peaks' broadening, suggest that the LSMO thin film is nanostructured in nature, in agreement with the local constrain induced by the SiO_2 surface.

Also depicted in Fig. 1a, BFO/LSMO/SOS XRD patterns exhibit an evolution in the growth of the BFO thin films (indicated with the + symbol) as function of its thickness (t_{BFO}). Details of such behavior are illustrated in Fig. 1b as linear scale plots of raw XRD data for several intervals. Furthermore, the data suggest that BFO films follow the (012) preferential growth orientation of the LSMO film showing good crystalline structure compatibility between both films in accordance with previous reports of BFO/LSMO stacks grown on substrates such as STO [11-16, 21] and silicon integrated STO/MgO/TiN/SOS [17]. This is in line with the rhombohedral symmetry reported for BFO (Fig. 2b) but belonging to the $R3c$ space group (SG 161) where, contrary to LSMO, the Bi^{3+} ions occupying the *A* site have an octahedral six-fold coordination as do the Fe^{3+} ions in the octahedral *B* site [29,30]. Moreover, BFO films show marked peaks shifted to lower angles (respect to those of the L40 sample) whose intensities increase with the increase in t_{BFO}. Using the peaks positions for the thicker B140 sample, the hexagonal parameters a_{BFO} = 5.615 Å and c_{BFO} = 14.065 Å resulted similar to those reported for BFO monodomain single crystal by Kubel *et al* in the ICSD 109370 card (a = 5.5787 Å and c = 13.8688 Å) and close to those reported for BFO ceramic powders in the ICSD 186955 card by Kiyanagi et al (a = 5.6044 Å and c = 13.9525 Å) [29, 31]. Furthermore, the intensity ratios I(012)/I(024) are in good correspondence with those of the XRD patterns of the LSMO and BFO phases; i.e., while for LSMO the intensity of the $(024)_{LSMO}$ plane is higher due to the higher scattering power of La/Sr ions, for BFO the intensity of the $(012)_{BFO}$ plane is higher due to the higher scattering power of Bi ions present in such planes (see Fig. 2b).

Meanwhile for the B50 sample the positions of the peaks for the BFO phase are closer to those of LSMO, for the B15 sample it is difficult to establish the presence of the ultrathin BFO layer. Nevertheless, its presence is verified by the small shift of the LSMO peaks at higher angles. This suggest that the lattice parameters of BFO for B15 and B50 are close to those of the LSMO layer. As can be seen in the bright field cross-section TEM image of Fig. 3b, a continuous BFO/LSMO interface is observed endorsing that the BFO film grew epitaxially incommensurate (with small lattice mismatch), inheriting both the *out-of-plane* orientation, the *in-plane* misorientation, and the nanostructured nature of the LSMO film. However, as a visible distinction, the BFO films exhibit clear contrasted nanoregions (shown in the HRTEM image in Fig. 3c) with an average size of ~ 4 nm, where grain boundaries are not noticeable. Moreover, the nanoregions preserve the same *out-of-plane* orientation (indicated by the dashed lines corresponding to the $(012)_{BFO}$ plane with interplanar distance of ~ 4.09 Å in agreement with the obtained a_{BFO} and c_{BFO} parameters) and have different *in-plane* orientations (illustrated in the HAADF image of Fig. 3d with a circle). Such contrasted nanoregions can be a result of the ferroelectric monodomains, making evident the multiferroic nature of the samples as will be discussed below.

Furthermore, Fig. 2b shows the BFO structure simulation where the (012) and (024) planes are described by the crossed Bi-O-Bi and Fe-O-Fe chains, respectively. Thus, it can be assumed that the BFO growth is induced by the LSMO surface in such manner that both Mn-O-Mn layers ($n(012)_{LSMO}$ planes) and La/Sr-O-La/Sr layers ($n(024)_{LSMO}$ planes) of the LSMO film constrain both the Bi-O-Bi layer ($n(012)_{BFO}$ planes) and the Fe-O-Fe layers ($n(024)_{BFO}$ planes) of the BFO film; depending on how the LSMO structure ends at the surface. As discussed in the following sections, this BFO-LSMO coupling is transcendental for the magnetic properties.

All these BFO/LSMO stacks features are different to those previously reported BFO/LSMO heterostructures where the BFO and LSMO structures are forced to grow with the perovskite symmetry (*Pm3m* or *R3m*), growing epitaxially cube-to-cube under compressive strain, and the lattice parameters (cubic or pseudo-cubic) are conditioned by those of the substrate such as STO or STO/MgO/TiN/Si(100) [11, 12, 14-17, 21].

The local chemical composition was investigated by STEM-EDX analysis. As an illustrative example, Fig. 3e shows the spectra obtained along a line scan on the cross-sectional surface of the B50 stack. All elements signals are present as expected and the BFO and LSMO layers limits are clearly identified. Additionally, the peaks indicated with the δ_1 symbol for the B140 stack and δ_2 for B50 and B70 stacks (Fig. 1b) are attributed to the $Bi_2Fe_4O_9$ parasite phase associated to Bi loss during the deposition processes [32]; other phases as γ-Fe_2O_3 were not detected. Nevertheless, due to its antiferromagnetic (AFM) nature, the presence of the $Bi_2Fe_4O_9$ compound (hardly detected in the B50 and B70 and not detected at all for B15 and B120) with reported Néel temperature of 260 K is not related with the ferromagnetic and ferroelectric phenomena discussed below; an assumption that agrees with that of Lahmar *et al* [32].

3.2. Magnetic properties of the LSMO/SOS substrate

Figure 4a shows the *in-plane* temperature dependence of zero-field-cooled (ZFC) and field-cooled (FC) magnetization (M) curves as function of the temperature for the L40 sample measured under an applied magnetic field (H) of 200 Oe. Preceding studies on LSMO films grown on dissimilar substrates have obtained ZFC curves exhibiting a FM behavior with Curie temperatures between 330 K to 360 K for thin films [14, 17, 21, 28, 33-35] and 370 K for bulks samples [36]. In contrast, the ZFC curve of the L40 sample shows a superparamagnetic (SP) behavior characterized by a paramagnetic(P)-SP transition at T_C = 196 K obtained from the M^{-1} vs T plot (inset of Fig. 4a), a blocking temperature of T_B = 53 K, and an irreversible temperature T_{irr} = 68 K close to T_B [37]. The SP behavior for LSMO systems have been reported in studies on 12 nm single-domain nanoparticles obtained by joint deposition [38] or 20 nm multidomain nanoparticles prepared via sol-gel [39]; but, to the best of our knowledge, such behavior in LSMO thin films have not been reported yet in the literature. Hence, this novel SP behavior is attributed to the nanostructured nature of the LSMO layer, constituted by FM single-domain nanoregions with critical size [37, 40-42] induced by the constrain of the SiO_2 surface as was discussed above. This SP behavior, is ascribed to weak inter-monodomain exchange between the inner FM magnetic moments which are shielded by the antiparallel exchange between the surface spin-glass layer at both sides of the inter-monodomain boundaries; however, it could disappear when the magnetic

field intensity overcomes the magnetic energy barrier associated with the surface anisotropic field at the boundaries. [37, 40-42]. Thus, we can expect that under high magnetic fields, the LSMO exhibit a classic FM behavior, but with a transition temperature below those reported in previous studies [28, 33-35]. In particular, Fig. 4b shows the high field FC curve obtained with a dc magnetic bias of 50 kOe where an anomaly is observed at 202 K, close to T_C = 196 K obtained from a low field ZFC curve, which could be associated to a second-order magnetic transition as that reported for $La_{0.67}Sr_{0.33}MnO_3$ [36].

Fig. 4c shows the *in-plane M* vs *H* hysteresis loops of the L40 sample measured after zero field cooling (from 400 to 2.5 K), at different temperatures, with a maximum applied magnetic field H_{max} = ± 40 kOe. As discussed above, the L40 sample exhibits typical FM loops with a coercive field (H_C) value of ~ 1100 Oe at 2.5 K that decreases with the increase in temperature reducing to 0 Oe above the observed T_C ~ 200 K (Fig.4a and 4c). The H_C values at lower temperatures are significantly higher than those reported (from 10 Oe to 500 Oe) for LSMO thin films grown on different substrates such as $LaAlO_3$(LAO) [34], $Ba_4Ti_3O_{12}$(BTO)/SOS and BTO/LAO/Si [33], $SrTiO_3$(STO) [12-14, 21, 34, 35], STO/MgO/TiN/SOS [17]. Similar temperature dependence of H_C is observed for the remanent (M_r) and maximum (M_{max}) magnetization values (inset of Fig. 4c). Moreover, the initial magnetization isotherms corresponding to the *M* vs *H* loops (Fig. 4d) illustrate that saturation is not reached as consequence of the nanostructured nature of the LSMO layer; additionally, they do not display the abrupt slope change characteristic of the first-order transition, instead, they exhibit a typical continuous change of the magnetic properties associated to a second-order transition [36].

3.3. Magnetic properties of the BFO/LSMO/SOS stacks

Figure 5a shows the *in-plane* temperature dependence of low field ZFC and FC magnetization curves for the BTO/LSMO/SOS stacks measured under an applied constant magnetic field of 200 Oe (the B70 response was omitted for clearness); the inset exhibits the areal normalized ZFC and FC curves for the B15 and B120 stacks which have identical areas in comparison with those areal magnetizations for the L40 sample. All samples exhibit a similar SP behavior resembling that of the L40 sample and strongly dependent of t_{BFO}, used as representative parameter of the volume fraction; while the net magnetization values

decrease when t_{BFO} increases, T_B and T_C shift to higher values. As can be seen, for the B120 and B140 samples with the thicker BFO layers, the magnetization values exhibit a significant drop, which can be attributed to the antiferromagnetic (AFM) order of the BFO present in a higher volume fraction. This result disagrees with the report of Wang *et al* [21], where the thickness effect of the BFO layer (changing from 150 to 600 nm) in epitaxial BFO/LSMO/STO heterostructures does not change significantly their low field FC response ascribed to the LSMO layer. However, it is worth noting that for B15 and B50, where the structural parameters of BFO films are constrained by those of LSMO, a significant magnetization is observed in the temperature range between 250 K and 400 K where the LSMO is in paramagnetic state. The latter is taken as indicative that these thinner BFO layers exhibit a ferromagnetic or ferrimagnetic ordering of the Fe magnetic moments.

This result establishes an important distinction with respect to other reports on epitaxial BFO/LSMO heterostructures grown on STO and integrated on Si(100) where the enhancement of magnetization is attributed to the magnetic exchange coupling at the AFM/FM interface but where the BFO layer remains antiferromagnetic [11, 13, 15, 17, 21]. Additionally, Fig. 5b shows the high field FC measurements obtained under a DC magnetic field bias of 50 kOe. The results confirm the effect of the thickness in the properties of the BFO layers as described above. As can be appreciated, the B15 sample exhibits an interesting interlayer interaction in all temperature range, made evident by the anomalies observed around 200 K (associated to the occurrence of magnetic phase transitions in both BFO and LSMO layers) and a significant increase of the magnetization at higher temperatures respect to the L40 sample.

To evaluate the individual contribution of the BFO and LSMO in the full stacks response, Fig. 6a, 6b, and 6c show representative *in-plane M* vs *H* hysteresis loops of the B15, B50, and B140 samples, respectively, measured after a zero field cooling (from 400 to 2.5 K), at different temperatures, with a maximum applied magnetic field $H_{max} = \pm 40$ kOe. The *M* vs *H* loops for B140 sample (similar result are observed for B70 and B120) show that hysteresis keeps the characteristic FM sigmoidal shape in all temperature range, following the behavior of the L40 sample (Fig. 4c), as can be seen in Fig. 6c. Figure 6d illustrates a comparison between the *M* vs *H* loops at 2.5 K of the volume magnetization (left) for all samples and of

the areal magnetization (right) for the B15 and B120 stacks. As can be seen in Fig. 6d, the M_{max} and M_r values decrease as the BFO thickness increases (10 fold reduced respect to those of the L40 sample for the thicker B140 sample), in correspondence with the M vs T curves behavior in Figs. 5a and 5b. In the meantime, as is expected, the areal normalized magnetization in the M vs T curves (inset of Fig. 5a) and in the M vs H loops (Fig. 6d) also decrease when t_{BFO} increases, while the BFO layer reaches greater volume fraction, regardless if the BFO displays the observed ferromagnetic or antiferromagnetic behavior.

Here, a *goose-neck* effect in the magnetic loops is displayed only for the B15 and B50 samples. To the best of knowledge, this behavior has not been reported in the literature for BFO/LSMO heterostructures. This distorted-sigmoidal shaped hysteresis loops in Fig. 6a and 6b, could result from the presence of more than one magnetic phase, where one of the phases switches at lower coercive field and the others at higher values [18, 43-46]. In such multiphase system, the transition from a low coercive field phase (soft phase) to a high coercive field phase (hard phase) in the magnetic hysteresis depends mainly on the exchange field [44] and the temperature [46], i.e. the magnetic layers can rotate freely without interlayer exchange coupling (IEC) or their magnetization states are under strong IEC [46]. Similar goose-neck effect has been observed in previous studies on hard/soft magnetic Sm-Co/Fe heterostructures [43], and on bilayers of Prussian blue analogues [18] where the magnetic behavior was explained in terms of an exchange-spring magnet; also in studies of fully epitaxial Fe_3O_4/MgO/Fe_3O_4/NiO/MgO(100) stacks where the strength and even the sign of the IEC are defined by charge-orbital ordering which changes the magnetization states of the spin valve [46].

In the hysteresis loops for the B15 and B50 samples (Figs. 6a and 6b), considering the hysteresis loops of the L40 sample (Fig. 4c), is possible to note the effect of a IEC phenomenon between two-phase magnetic materials. In this case, between the LSMO layer and a FM BFO layer whose behavior, up to now, has not been reported before for BFO compounds. Figs. 6a and 6b show that even though the M_{max}, M_r, and H_C values decrease with temperature following the same behavior of the L40, the initial distorted-sigmoidal shape at 2.5 K exhibits a shrinking of the neck (near $H = 0$) but the loops preserve the shape and its area at the higher magnetic field values. However, when the temperature rises beyond

100 K the neck in the loops displays a sharp increase of the coercivity. Meanwhile, in Fig 6e for the B15 sample, the initial magnetization isotherms exhibit a temperature-independent abrupt slope change at 4.7 kOe, indicative of an apparent coercive field, with a constant increase of magnetization of $\Delta M \sim 30$ emu/cm^3 at temperatures below the P-SP transition temperature of the LSMO layer. Additionally, the temperature-dependence of the H_C values for B15 and B50 is illustrated in Fig. 6f and compared with those of the L40 sample. The comparison between the M vs H loops of the L40, B15, and B50 samples at 2.5 K and 300 K is shown in Fig. 6g and 6h respectively. As can be seen, at lower temperature the H_C values for the B15 and B50 stacks are close to those of L40 while for temperatures between 40 K and 100 K they are appreciably higher. Also, the B15 and B50 stacks exhibit higher H_C values (Fig. 6f) at room temperature (1600 and 1830 Oe as average, respectively) with respect to those at 2.5 K (1100 and 1240 as average) attributed to the now considered ferromagnetic nature of the BFO layers, characterized by a Curie temperature above 400 K, according to the behavior of the H_C values shown in Fig. 6f. The observed coercivity reduction (~ 30 % obtained from the H_C at 2.5 K and 300 K), here associated to the high field BFO layer, has been also reported for the coercivity of the hard or high field phase in metal heterostructures such as Sm-Co/Fe [43], in bilayers of Prussian blue analogues [18], or in composites like $BaFe_{12}O_{19}/CoMn_{0.1}Fe_{1.9}O_4$ [45]. These H_C values are significantly higher than those reported for BFO/LSMO stacks grown on substrates such as STO [12-14, 21] and silicon integrated STO/MgO/TiN/SOS [17,19], where the BFO exhibits the typical AFM behavior. Thus, it can be assumed that the properties shown by the B15 and B50 samples are a consequence of a strong IEC between the LSMO phase and the BFO phase with similar coercive values, which vanishes when the LSMO layer undergoes a transition to its paramagnetic state near 200 K, in correspondence with the second-order magnetic transition discussed above. The similarity of the intrinsic parameters values and magnetic behavior in B15 and B50 samples confirm that the BFO layers have the same FM phase.

Taking into account the results discussed above related to the magnetic behavior of the B15 and B50 stacks below 200 K and in particular, that the ferromagnetic BFO and LSMO phases have coercive fields differing only in 30 %, it is difficult to deconvolute the contributions when such phases are strongly interacting [43]. In order to evaluate the individual contribution of BFO and LSMO and the nature of the observed interlayer exchange coupling,

measurements of the magnetization reversal and reversibility processes were carried out. Fig. 7 shows the minor M vs H loops of B15 sample measured at 2.5 K, after the major loop obtained at ± 40 kOe, for several values of the maximum reverse magnetic field (H_{rev}) ranging from -1.2 kOe (above but near the coercive field of the LSMO layer) up to -8 kOe. As can be seen, although the minor loop of H_{rev} = -1.2 kOe corresponds to the overall layers stack, its behavior can be associated to the LSMO layer where only a small volume fraction of the reversible domains are switched as is indicated for the positive value of M at H = 0, and the reversal field is smaller than the coercive field of the BFO layer (~ 1.6 kOe). For the minor loops with H_{rev} values of -1.6 kOe and -3.0 kOe the M shows negative values at H = 0, but their curves converge with the first minor loops. Thus, up to H_{rev} = -3.0 kOe the minor loops are not fully reversible, so the magnetization of LSMO layer cannot rotate freely [46] and thus it can be established that the observed IEC is not only restricted to the interface as it occurs in the exchange-spring magnets [43]. However, the occurrence of exchange coupling is not discarded in the BFO/LSMO interface.

For the minor loop corresponding to H_{rev} = -4.8 kOe (slightly higher than the 4.7 kOe value indicated in the initial isotherms in Fig. 6e), although the loop does not reach the major loop it exhibits the goose-neck shape. This could be a consequence of the propagation of the domain wall in the low field LSMO layer compressed against the interface with the high field BFO layer, which initiates the magnetization reversal process in the BFO reducing its coercive field as was discussed above in the global analysis [18]. Such behavior illustrates that the magnetization of the BFO layer cannot rotates freely either. Finally, the minor loop corresponding to H_{rev} = -8.0 kOe repeats very closely the major loop, which can be an evidence that the BFO layer switches irreversibly at H_{irr} ~ -6.0 kOe [43]. The differences in the loop values can be associated to the fact that, under -8.0 kOe, the M_{max} value was not reached. It is worth noting that these results show the presence of two-phase FM stacks which exhibit parallel, antiparallel, or mixed magnetization states as function of the external magnetic field which would present interesting effects in the magnetoresistance response and could be successfully integrated to the silicon technology and applied in novel magnetoelectronics devices.

Up to this point, our experiments demonstrate that the thinner BFO films (15 and 50 nm thicknesses) grown on LSMO/SOS substrates exhibit a ferromagnetic behavior, with a Curie temperature above to 400 K. Such ferromagnetic ordering in the BFO films can be explained, on the base of the Goodenough theory [47], aimed at the establishment of a novel electronic-spin configuration in the Fe^{3+}-O-Fe^{3+} sublattice where the Fe-O bonds are alternately semicovalent or ionic, in such manner that, while the net magnetic moment associated with the O^{2-} ions is antiparallel with the net moment of the neighboring Fe^{3+} ions, the Fe^{3+} ions moments in the consecutive octahedra remain ferromagnetically coupled. Here, we propose that the origin of such ferromagnetic ordering of the Fe^{3+}-O-Fe^{3+} sublattice is induced, by strong hybridization at the LSMO surface during the growth processes in agreement with the crystallographic analysis discussed above, as consequence of superexchange coupling interactions between the Fe^{3+} ions with the ferromagnetic Mn^{3+}-O-Mn^{3+}/Mn^{4+} sublattice regulated by a double-exchange mechanisms where, according with the $La_{0.7}{}^{3+}Sr_{0.3}{}^{2+}(Mn_{0.7}{}^{3+}Mn_{0.3}{}^{4+})O_3$ stoichiometry, the Mn^{4+} ions are diluted in the matrix surrounded by the larger number of Mn^{3+} ions found in LSMO compounds [12, 47]. It is worth to note that for this Mn^{4+} concentration, the Mn^{3+}-O and Mn^{4+}-O bonds having different lengths, produce a cooperative elastic strain with rhombohedral symmetry [47]. This leads to a strong FM superexchange coupling between the Fe^{3+}-O-Fe^{3+} array and the Mn^{3+}-O-Mn^{3+}/Mn^{4+} array through the $d_x{}^2{}_{-y}{}^2$ orbital ordered in the respective $n(024)_{BFO}$ and $n(012)_{LSMO}$ planes, where antiparallel magnetizations are expected at both sides of the interface [3, 12, 47]. This models of superexchange interactions and the coupling mechanism through $d_x{}^2{}_{-y}{}^2$ orbital ordering were presented by Yu et al [3, 12] to explain the ferromagnetism observed in the AFM BFO related to an electronic orbital reconstruction at the interface of BFO/LSMO heterostructures strongly strained by the cubic STO substrate. However, in this case there is definite distinction: the FM order formation is extended through all the bulk of the sample, as a consequence of the BFO structure acquiring the same rhombohedral symmetry and growth orientation of the LSMO in turn induced by the SiO_2 surface of the silicon wafer.

3.4 Ferroelectric and piezoelectric properties of the BFO/LSMO/SOS stacks

Piezoresponse force microscopy (PFM) in resonance mode was used to study the ferroelectric and piezoelectric properties of the BFO films. Within the section, the results for the B50 and

B140 will be discussed, as those are representative for the rest of the stacks. The polarization switching patterns were explored in a DC regime working at optimal applied voltages. Here, an *out-of-plane* polarization screening by electric bias scanning was realized as follows on B50 (B140) sample. An initial poling was carried out by applying a bias of -9 V (-32 V) DC in a concentric 8 × 8 μm^2 inner area, followed by applying +6 V (+32 V) DC in a concentric 4 × 4 μm^2 area enclosed within the previous one. After poling, topography, amplitude, and phase PFM images were simultaneously taken on the full 12 × 12 μm^2 area. The results are shown in the Figs. 8a-8c for B50 and Figs. 8e-8g for B140. In the topography images of B50 (Fig. 8a) and B140 (Fig. 8e) no damage was observed as result of the applied electric fields, indicating that the collected PFM signals were purely coming from of the BFO layers piezoresponse. Additionally, roughness values of 8.27 nm (B50) and 2.85 nm (B140) were measured, in good correspondence with the observed results by cross-sectional TEM. As can be seen, the concentric square patterns in the amplitude piezoresponses (Figs. 8b and 8f) show well defined perimeter borders, separating regions with similar expansion and contraction amplitude values, associated to FE domain walls (DW); while, the corresponding concentric patterns in the phase piezoresponse (Figs. 8c and 8f) show well defined bright and dark contrast corresponding to *up* and *down* FE domain, respectively, i.e., domains with opposite polarization switched along the *out-of-plane* orientation [48,49]. Moreover, the phase profile in Figs. 8d and 8h shows that the FE domain structure in the B50 and B140 samples is characterized by 180º and 109º DWs in good agreement with previous detailed studies on epitaxial BFO films [48-51]. In particular, the 109º DWs are typical of the rhombohedral symmetry once the spontaneous polarization lies along the [111] direction in the BFO structure by the large displacement of the Bi ions relative to FeO_6 octahedra (Fig. 2b) [52]. The asymmetry in the electric bias values (Fig. 8c) and the display of the 180º DWs switching in the B50 sample, having the same preferential orientation of the B140 sample, could be related to a rearrangement of the ferroelectric distortion strongly related with the ferromagnetic array. This could result from the spin-crossover phenomenon associated with the magnetic centers in high-spin and low-spin states of the d^5–Fe ions at the octahedra, predicted by Bersuker using the pseudo Jahn-Teller effect theory applied to multiferroics with like-perovskite structures [53].

Furthermore, polarization hysteresis loops through the phase vs DC voltage curves and the

strain loops through the displacements amplitude vs DC voltage curves (butterfly loops) were recorded to obtain quantitative information of the FE domain structure and their electromechanical properties. Such measurements were done with a pulsed triangular DC voltage signal in the ON and OFF field modes; however, as in the ON field mode the loops contain the electromechanical and electrostatic effects induced by the capacitive force between the cantilever and the sample surface, only the OFF field mode response was used to minimize such effects [54,55]. Thus, Fig. 9a and 9c show the phase and butterfly loops for the B50 and B140, respectively. The phase loop for B50 exhibits a squared loop typical of 180º DWs as was observed before with a coercive field of ~ 3.7 V (740 kV/cm), while for the B140 sample shows an inclined phase loop with lower coercive field of ~ 2.8 V (200 kV/cm) in correspondence with the observed 109º DWs. The coercive field value of the B50 sample is similar to those of previous studies on epitaxial BFO thin films [19, 49]. Furthermore, from the typical butterfly loops the values of piezoelectric constant d_{33} = 23 pm/V for B50 and d_{33} = 55 pm/V for B140 were calculated and are in good agreement with the d_{33} thickness dependence previously reported in epitaxial BFO films grown on STO substrate [56].

Finally, to distinguish if the observed switching processes, hysteresis loops, and electromechanical properties are originated from the spontaneous polarization, the first/second harmonic criterion was used [57, 58]. This criterion establishes that for FE samples, under an AC excitation the amplitude of the first harmonic (obtained around of the resonant frequency of the cantilever-specimen system, ω_0) is higher than that of the second harmonic (obtained around to $\omega_0/2$) [58]. As can be seen in Figs 9b and 9d, the amplitude of the first harmonic is notably higher than that of the second harmonic for both B50 and B140 samples.

Conclusions

Highly textured multiferroic $BiFeO_3/La_{0.7}Sr_{0.3}MnO_3$ thin film stacks were successfully grown on SiO_2/Si(100) substrates by rf-magnetron sputtering, with different BFO layer thicknesses (15, 50, 70, 120, and 140 nm). The 40 nm LSMO layers grew nanostructured, presenting FM single-domain nanoregions induced by the constrain of the SiO_2 surface, and exhibiting a superparamagnetic behavior at low magnetic field. At the same time, the BFO film grew epitaxially nanostructured, inheriting the *out-of-plane* orientation and the *in-plane*

misorientation of the LSMO film. The BFO layers with greater volume fraction (thickness >70 nm) show the typical antiferromagnetic behavior. The thinner BFO layers display a novel ferromagnetic behavior characterized by a new magnetic configuration in the Fe^{3+}-O-Fe^{3+} sublattice, induced by strong hybridization as consequence of superexchange coupling interactions with the ferromagnetic Mn^{3+}-O-Mn^{3+}/Mn^{4+} sublattice of LSMO. All BFO layers show excellent ferroelectric and piezoelectric properties, exhibiting typical 180º and 109º DWs structure depending on film thickness. The FM and FE coexistence and the strong magnetic interlayer exchange coupling in such BFO/LSMO/SiO_2/Si system envisage its potential applications in new magneto-electronic devices with the advantage of using the ion sputtering film-growth technique of common use in present day technology.

Acknowledgements

This work was supported by DGAPA-UNAM Grants (IN110315 and IN106414) and Conacyt Grants (127633 and 166286). The authors thank the technical support from CIQA (Saltillo), the Laboratorio Nacional de Investigaciones en Nanociencias y Nanotecnología (LINAN, IPICyT), and the Laboratorio Nacional de Nanotecnología (CIMAV-Chihuahua), in Mexico. The authors thank the technical assistance from A.G. Rodriguez, E. Murillo, E. Aparicio, P. Casillas, I. Gradilla, F. Ruiz, J. López-Mendoza, G.F. Hurtado (CIQA), O.O. Solís and J.G. Murillo-Ramírez (CIMAV-Chihuahua). C.F. Sánchez-Valdés thanks CTIC-UNAM for supporting his postdoctoral position at CNyN-UNAM.

REFERENCES

[1] C. Lu, W. Hu, Y. Tian, and T. Wu, Multiferroic oxide thin films and heterostructures, Appl. Phys. Rev. 2 (2015) 021304.

[2] C.A.F. Vaz, Electric field control of magnetism in multiferroic heterostructures, J. Phys.: Condens. Matter 24 (2012) 333201.

[3] P. Yu, Y.H. Chu, and R. Ramesh, Oxide interfaces: pathways to novel phenomena. Review, Materials Today 15 (2012) 320-327.

[4] J.M. Hu, T. Nan, N.X. Sun, L.Q. Chen, Multiferroic magnetoelectric nanostructures for novel device applications, MRS Bulletin 40 (2015) 728-735.

[5] V. Garcia, M. Bibes, A. Barthélémy, Artificial multiferroic heterostructures for electric control of magnetic properties, C. R. Physique 16 (2015)168-181.

[6] B. Cui, C. Song, H. Mao, Y. Yan, F. Li, S. Gao, J. Peng, F. Zeng, F. Pan. Manipulation of Electric Field Effect by Orbital Switch. Adv. Funct. Mater. 26 (2016) 753–759.

[7] E.Y. Tsymbal, A. Gruverman, V. Garcia, M. Bibes, A. Barthélémy, Ferroelectric and multiferroic tunnel junctions, MRS Bulletin 37 (2012) 138-143.

[8] Y. Zhu, P. Liu, R. Yu, Y.H. Hsieh, D. Ke, Y.H. Chuc, and Q. Zhan, Orientation-tuning in self-assembled heterostructures induced by a buffer layer, Nanoscale 6 (2014) 5126–5131.

[9] N.M. Aimon, D.H. Kim, X.Y. Sun, and C.A. Ross, Multiferroic behavior of templated $BiFeO_3$–$CoFe_2O_4$ self-assembled nanocomposites, ACS Appl. Mater. Interfaces 7 (2015) 2263–2268.

[10] D.H. Kim, X.Y. Sun, T.C. Kim, Y.J. Eun, T. Lee, S.G. Jeong, and C.A. Ross, Magnetic phase formation in self-assembled epitaxial BiFeO3−MgO and BiFeO3−MgAl2O4 nanocomposite films grown by combinatorial pulsed laser deposition, ACS Appl. Mater. Interfaces 8 (2016) 2673–2679.

[11] M. Huijben, P. Yu, L. W. Martin, H. J. A. Molegraaf, Y-H Chu, Mikel Holcomb, N. Balke, G. Rijnders, and R. Ramesh. Ultrathin limit of exchange bias coupling at oxide multiferroic/ferromagnetic interfaces. Adv. Mat. 25, 34 (2013) 4739-4745.

[12] P. Yu, J.S. Lee, S. Okamoto, M.D. Rossell, M. Huijben, C.H. Yang, Q.He, J.X. Zhang, S.Y. Yang, M.J. Lee, Q.M. Ramasse, R. Erni, Y.H. Chu, D.A. Arena, C.C. Kao, L.W. Martin, and R. Ramesh, Interface ferromagnetism and orbital reconstruction in $BiFeO_3$−$La_{0.7}Sr_{0.3}MnO_3$ heterostructures, Phys. Rev. Lett. 105 (2010) 027201.

[13] M. Vafaee, S. Finizio, H. Deniz, D. Hesse, H. Zabel, G. Jakob, M. Klaui, The effect of interface roughness on exchange bias in $La_{0.7}Sr_{0.3}MnO_3$-$BiFeO_3$ heterostructures, Appl. Phys. Letters 108 (2016) 072401.

[14] V. Kumar, A. Gaur, R.J. Choudhary, M. Gupta, Surface and grain boundary interdiffusion in nanometer-scale LSMO/BFO bilayer, J. Magnetism and Magnetic Mater. 405 (2016) 72–77.

[15] S. Singh, J.T. Haraldsen, J. Xiong, E.M. Choi, P.Lu, D. Yi, X.D. Wen, J. Liu, H. Wang, Z. Bi, P. Yu, M.R. Fitzsimmons, J.L. MacManus-Driscoll, R. Ramesh, A.V. Balatsky, J.X. Zhu, and Q. X. Jia, Induced Magnetization in $La_{0.7}Sr_{0.3}MnO_3/BiFeO_3$ Superlattices, Phys. Rev. Lett. 113 (2014) 047204.

[16] S.M. Wu, S. A. Cybart, D. Yi, J.M. Parker, R. Ramesh, and R.C. Dynes, Full electric control of exchange bias, Phys. Rev. Lett. 110 (2013) 067202.

[17] S.S. Rao, J.T. Prater, F. Wu, C.T. Shelton, J.P. Maria, J. Narayan, Interface Magnetism in Epitaxial $BiFeO_3$-$La_{0.7}Sr_{0.3}MnO_3$ Heterostructures Integrated on Si(100), Nano Lett. 13 (2013) 5814−5821.

[18] J.P. Prieto-Ruiz, F.M. Romero, H.Prima-Garcıa, and E. Coronado, Exchange coupling in an electrodeposited magnetic bilayer of Prussian blue analogues, J. Mater. Chem. C 3 (2015) 11122.

[19] S.R. Singamaneni, J.T. Prater, S. Nori, D. Kumar, B. Lee, V. Misra, and J. Narayan, Ferroelectric and magnetic properties of multiferroic $BiFeO_3$-$La_{0.7}Sr_{0.3}MnO_3$ heterostructures integrated with Si (100), J. Appl. Phys. 117 (2015) 17D908.

[20] S.R. Singamaneni, W. Fan, J.T. Prater, and J. Narayan, Magnetic properties of $BaTiO_3/La_{0.7}Sr_{0.3}MnO_3$ thin films integrated on Si(100), J. Appl. Phys. 116 (2014) 224104.

[21] L. Wang, Z. Wang, K.J. Jin, J.Q. Li, H.X. Yang, C. Wang, R.Q. Zhao, H.B. Lu, H.Z. Guo, and G.Z. Yang, Effect of the thickness of $BiFeO_3$ layers on the magnetic and electric properties of $BiFeO_3/La_{0.7}Sr_{0.3}MnO_3$ heterostructures, Appl. Phys. Lett. 102 (2013) 242902.

[22] A. Chen, Z. Bi, C.F. Tsai, J.H. Lee, Q.S., X.Z., Q. Jia, J.L. MacManus-Driscoll, and H. Wang, Tunable low-field magnetoresistance in $(La_{0.7}Sr_{0.3}MnO_3)_{0.5}$:$(ZnO)_{0.5}$ self-assembled vertically aligned nanocomposite thin films, Adv. Funct. Mat. 21 (2011) 2423-2429.

[23] J.H. Park, E. Vescovo, H.J. Kim, C. Kwon, R. Ramesh, T. Venkatesan. Direct evidence for a half-metallic ferromagnet. Nature 392 (1998) 794-796.

[24] Putz H, Brandenburg K. Diamond-Crystal and Molecular Structure Visualization, Crystal Impact. Kreuzherrenstr, 102, 53227 Bonn, Germany. http://www.crystalimpact.com/diamond.

[25] .J. Hibble, S.P. Cooper, A.C. Hannon, I.D. Fawcett, and M. Greenblatt, Local distortions in the colossal magnetoresistive manganates $La_{0.70}Ca_{0.30}MnO_3$, $La_{0.80}Ca_{0.20}MnO_3$ and $La_{0.70}Sr_{0.30}MnO_3$ revealed by total neutron diffraction, J. Phys.: Condens. Matter 11 (1999) 9221–9238.

[26] U. Khalilov, E.C. Neyts, G. Pourtois, A.C.T. van Duin, Can We Control the Thickness of Ultrathin Silica Layers by Hyperthermal Silicon Oxidation at Room Temperature?, J. Phys. Chem. C 115 (2011), 24839–2484.

[27] K. Awazu and H. Kawazoe, Strained Si–O–Si bonds in amorphous SiO2 materials: A family member, of active centers in radio, photo, and chemical responses, J. Appl. Phys. 94 (2003) 6243-6262.

[28] C. Adamo, L. Méchin, T. Heeg, M. Katz, S. Mercone, B. Guillet, S. Wu, J.M. Routoure, J. Schubert, W. Zander, R. Misra, P. Schiffer, X.Q. Pan, and D.G. Schlom, Enhanced electrical and magnetic properties in La0.7Sr0.3MnO3 thin films deposited on CaTiO3-buffered silicon substrates, APL Materials 3, (2015) 062504.

[29] F. Kubel and H. Schmid, Structure of a Ferroelectric and Ferroelastic Monodomain Crystal of the Perovskite $BiFeO_3$, Acta Cryst. B46 (1990), 698-702.

[30] S. T. Zhang, M. H. Lu, D. Wu, Y. F. Chen, and N. B. Ming, Larger polarization and weak ferromagnetism in quenched Bi Fe O 3 ceramics with a distorted rhombohedral crystal structure, Appl. Phys. Lett. 87 (2005) 262907

[31] R. Kiyanagi, T. Yamazaki, Y. Sakamoto, H. Kimura, Y. Noda, K. Ohyama, S. Torii, M. Yonemura, J. Zhang, and T. Kamiyama, Structural and Magnetic Phase Determination of (1-x)BiFeO3–xBaTiO3 Solid Solution, J. Phys. Soc. Jpn. 81 (2012) 024603.

[32] A. Lahmar, K. Zhao, S. Habouti, M. Dietze, C.H. Solterbeck, M. Es-Souni, Off-stoichiometry effects on BiFeO3 thin films, Solid State Ionics 202 (2011) 1–5.

[33] J.Y. Gu, C. Kwon, M.C. Robson, Z. Trajanovic, K. Ghosh, R.P. Sharma, R. Shreekala, M. Rajeswari, T. Venkatesan, R. Ramesh, and T. W. Noh. Growth and properties of c -axis textured $La_{0.7}Sr_{0.3}MnO_{3-\delta}$ films on SiO_2/Si substrates with a $Bi_4Ti_3O_{12}$ template layer, Appl. Phys. Lett. 70 (1997) 1763.

[34] A.M. Haghiri-Gosnet, J. Wolfman, B. Mercey, Ch. Simon, P. Lecoeur, M. Korzenski, M. Hervieu, R. Desfeux, and G. Baldinozzi, Microstructure and magnetic properties of strained $La_{0.7}Sr_{0.3}MnO_3$ thin films, J. Appl. Phys. 88 (2000) 4257.

[35] D. Hunter, J.B. Dadson, K. Zhang, B. Lasley, K. Lord, T.M. Williams, R.R. Rakhimov, A. K. Pradhan, J. Zhang, and D.J. Sellmyer, Self-assembled nanocrystalline epitaxial manganite films on $SrTiO_3$/Si heterostructures, J. Appl. Phys. 99 (2006) 08Q307.

[36] J. Mira and J. Rivas, Change from first- to second-order magnetic phase transition in $La_{2/3}CaSr_{1/3}MnO_3$ perovskites, Phys. Rev. B 60 (1999) 2998-3001.

[37] M. Knobel1, W.C. Nunes, L.M. Socolovsky, E. De Biasi, J.M. Vargas, and J.C. Denardin, Superparamagnetism and Other Magnetic Features in Granular Materials: A Review on Ideal and Real Systems, J. Nanosci. Nanotechnol. 8 (2008) 2836–2857.

[38] V.N. Krivoruchko, A.I. Marchenko, and A.A. Prokhorov, Superparamagnetic resonance of single-domain nanoparticles of $LaSrMnO_3$, Low Temperature Physics 33 (2007) 433.

[39] A. Rostamnejadi, H. Salamati, P. Kameli, H. Ahmadvand, Superparamagnetic behavior of La0.67Sr0.33MnO3 nanoparticles prepared via sol–gel method, J. Magn. Magn. Mater. 321 (2009) 3126–3131.

[40] C.T. Hsieh, J.T. Lue, Anisotropy-induced quantum superparamagnet state in cobalt-ferrite nanoparticles at low temperatures, Phys. Lett. A 316 (2003) 329–335.

[41] W. Zheng, P. Kumar, A. Washington, Z. Wang, N.S. D. Geoffrey, F. Strouse, and K. Singh, Quantum Phase Transition from Superparamagnetic to Quantum Superparamagnetic State in Ultrasmall $Cd_{1-x}Cr(II)_xSe$ Quantum Dots?, J. Am. Chem. Soc. 134 (2012) 2172–2179.

[42] C. Xiao, J. Zhang, J. Xu, W. Tong, B. Cao, K. Li, B. Pan, H. Su, and Y. Xie, Quantum Tunneling of Magnetization in Ultrasmall Half-Metallic V3O4 Quantum Dots: Displaying Quantum Superparamagnetic State, Scientific Reports, 2 (2012) 755.

[43] E.E. Fullerton, J.S. Jiang, S.D. Bader, Hard/soft magnetic heterostructures: model exchange-spring magnets, J. Magn. Magn. Mater. 200 (1999) 392-404

[44] A. Raghunathan, Y. Melikhov, J.E. Snyder, D.C. Jiles, Modeling of two-phase magnetic materials based on Jiles–Atherton theory of hysteresis, J. Magn. Magn. Mater. 324 (2012) 20–22.

[45] N.P. Gaunkar, O. Kypris, I.C. Nlebedim, and D.C. Jiles. Analysis of barkhausen noise emissions and magnetic hysteresis in multi-phase magnetic materials, IEEE Transactions on Magnetics 50:11 (2014) 7301004.

[46] H.C. Wu, O.N. Mryasov, M. Abid, K.Radican, I.V. Shvets, Magnetization States of All-Oxide Spin Valves Controlled by Charge-orbital Ordering of Coupled Ferromagnets, Scientific Reports, 3 (2013) 1830

[47] J.B. Goodenough, Theory of the role of covalence in the perovskite-type manganites, Phys. Rev. 100 (1955) 564-571.

[48] L. Chen, Z. Cheng, W. Xu1, X. Meng, G. Yuan, J. Liu, and Z. Liu, Electrical and mechanical switching of ferroelectric polarization in the 70 nm BiFeO3 film, Scientific Reports, 6 (2016) 19092.

[49] Y.H. Chu, Q. Zhan, L. W. Martin, M.P. Cruz, P. L. Yang, G.W. Pabst, F. Zavaliche, S.Y. Yang, J.X. Zhang, L.Q. Chen, D.G. Schlom, I.N. Lin, T.B. Wu, and R. Ramesh, Nanoscale domain control in multiferroic $BiFeO_3$ thin films, Adv. Mater. 18 (2006) 2307–2311.

[50] Y. Jin, X. Lu, J. Zhang, Y. Kan, H. Bo, F. Huang, T. Xu, Y. Du, S. Xiao, and J. Zhu, Studying the polarization switching in polycrystalline $BiFeO_3$ films by 2D piezoresponse force microscopy, Scientific Reports, 5 (2015) 12237.

[51] S.H. Baek and C.B. Eom, Reliable polarization switching of $BiFeO_3$, Phil. Trans. R. Soc. A (2012) 370, 4872–4889.

[52] F. Zavaliche, S.Y. Yang, T. Zhao, Y.H. Chu, M.P. Cruz, C. B. Eom, and R. Ramesh, Multiferroic BiFeO3 films: domain structure and polarization dynamics, Phase Transitions 79 (2006) 991–1017.

[53] I.B. Bersuker pseudo Jahn-Teller origin of perovskite multiferroics, magnetic-ferroelectric crossover, and magnetoelectric effects: the d^0-d^{10} problem, Phys. Rev. Lett. 108 (2012) 137202.

[54] S. Hong, H. Shin, J. Woo, and K. No, Effect of cantilever–sample interaction on piezoelectric force microscopy, Appl. Phys. Lett. 80 (2002) 1453.

[55] S. Hong, J. Woo, H. Shin, J.U. Jeon, Y. E. Pak, E.L. Colla, N. Setter, E. Kim, and K. No. Principle of ferroelectric domain imaging using atomic force microscope. J. Appl. Phys. 89 (2001) 1377.

[56] J. Wang, J.B. Neaton, H. Zheng, V. Nagarajan, S.B. Ogale, B. Liu, D. Viehland, V. Vaithyanathan, D.G. Schlom, U.V. Waghmare, N.A. Spaldin, K.M. Rabe, M. Wuttig, R.

Ramesh, Epitaxial $BiFeO_3$ multiferroic thin film heterostructures, Science 299 (2003) 1719-1722.

[57] C. Harnagea, A. Pignolet, M. Alexe, and D. Hesse, Higher-order electromechanical response of thin films by contact resonance piezoresponse force microscopy, IEEE Transactions on Ultrasonics, Ferroelectrics, and Frequency Control 53:12 (2006) 2309-2322.

[58] Qian Nataly Chen, Yun Ou, Feiyue Ma, and Jiangyu Li, Mechanisms of electromechanical coupling in strain based scanning probe microscopy, Appl. Phys. Lett. 104 (2014) 242907.

Figure captions

Figure 1. (a) Comparison between the X-ray diffraction patterns of the BFO/LSMO/SOS stacks for different BFO thin film thickness: 15nm (B15), 50 nm (B50), 70 nm (B70), 120 nm (B120), and 140 nm (B140), and those of the LSMO/SOS sample with LSMO thin film of 40 nm thickness. (b) Patterns details in linear scale of the BFO/LSMO/SOS stacks. The + and * symbols indicate the peak positions of the BFO and LSMO phases respectively, and the δ symbol marks the peaks associated to a secondary phase.

Figure 2. Structural simulations obtained from the XRD data of the (a) LSMO and (b) BFO thin films as were deposited. The out-of-plane direction is indicated. In both cases, a representative region of (012) and (024) planes is illustrated.

Figure 3. Representative cross-sectional TEM images. Bright field micrographs of (a) LSMO film 40 nm thick on SiO_2/Si substrate and (b) the B15 stack (inside, a region of the BFO/LSMO interface in B50). (c) HRTEM of the BFO layer in the B50 stack; the spherical nanoregions have an average size of 4 nm. (d) HAADF images of nanoregions of the BFO layer in the B50 stack with small *out-of-plane* mismatch and *in-plane* orientations as the circle denotes. (e) STEM-EDX analysis on a 100 nm line scan on the B50 stack.

Figure 4. Magnetic characterization of 40 nm LSMO thin film. (a) Low field ZFC and FC curves obtained at 200 Oe; inset: M^{-1} vs T curve obtained from the ZFC measurement. (b) High field FC curve obtained at 50 kOe. (c) M vs H hysteresis loops measured at different temperatures with maximum magnetic field H_{max} = ± 40 kOe: inset: remanent M_r and maximum M_{max} magnetization dependence with temperature. (d) Virgin isotherms corresponding to the hysteresis loops in (c).

Figure 5. Magnetization as function of temperature (M vs T) plots for BFO/LSMO/SOS stacks with different BFO thin film thickness of: (a) low field ZFC (filled symbols) and FC curves (open symbols), H_{dc} = 200 Oe, (b) high field FC curves, H_{dc} = 50 kOe. The inset in (a) shows the areal normalized M vs T plots for B15 and B120 stacks with identical areas, in comparison with that of LSMO/SOS (L40) sample.

Figure 6. Magnetic characterization of BFO/LSMO/SOS stacks with different thickness of the BFO thin film. M vs H hysteresis loops measured at different temperatures with H_{max} =

± 40 kOe for (a) B15, (b) B50, and (c) B140 stacks. (d) Comparison between the *M* vs *H* loops of: (left) the volume magnetization for all samples and (right) the areal magnetization for the B15 and B120 stacks with identical areas. (e) Virgin isotherms taken from the hysteresis loops in (a). (f) Temperature dependence of the coercive magnetic field H_c for the B15 and B50 samples compared to those of the L40 sample. Comparison between the *M* vs *H* loops of B15, B50, and L40 at (g) 2.5 K and (h) room temperature (300 K).

Figure 7. *M* vs *H* loops for the B15 sample at 2.5 K. After the major loop obtained at ± 40 kOe, minor hysteresis loops were measured at different values of the maximum reverse magnetic field from -1.2 kOe near above H_C up to -8 kOe.

Figure 8. *Out-of-plane* PFM images after poling processes of (the bias voltages are indicated): topography of (a) B50 and (e) B140 samples, amplitude of (b) B50 and (f) B140, and phase of (c) B50 and (g) B140. Phase profile of (d) B50 and (h) B140 samples.

Figure 9. Phase-voltage and amplitude-voltage loops of (a) B50 and (c) B140 samples obtained in OFF field mode. First and second harmonic spectra of the (a) B50 and (c) B140 samples.

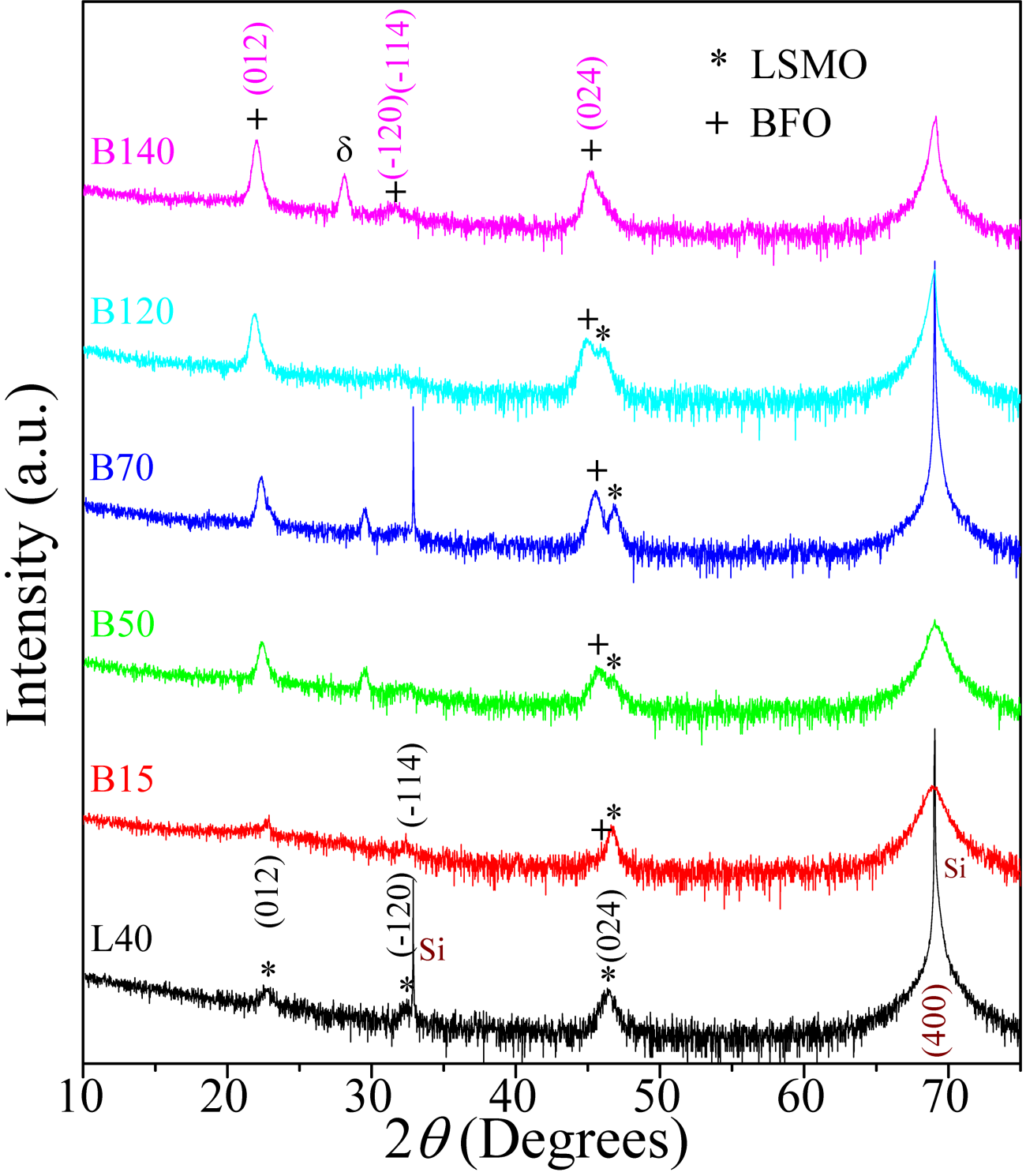
* LSMO
+ BFO
B140
B120
B70
B50
B15
L40
(012)
δ
(-120)(-114)
(024)
(-114)
(012)
(-120)
Si
(024)
Si
(400)
Intensity (a.u.)
10
20
30
40
50
60
70
2θ (Degrees)

(a)

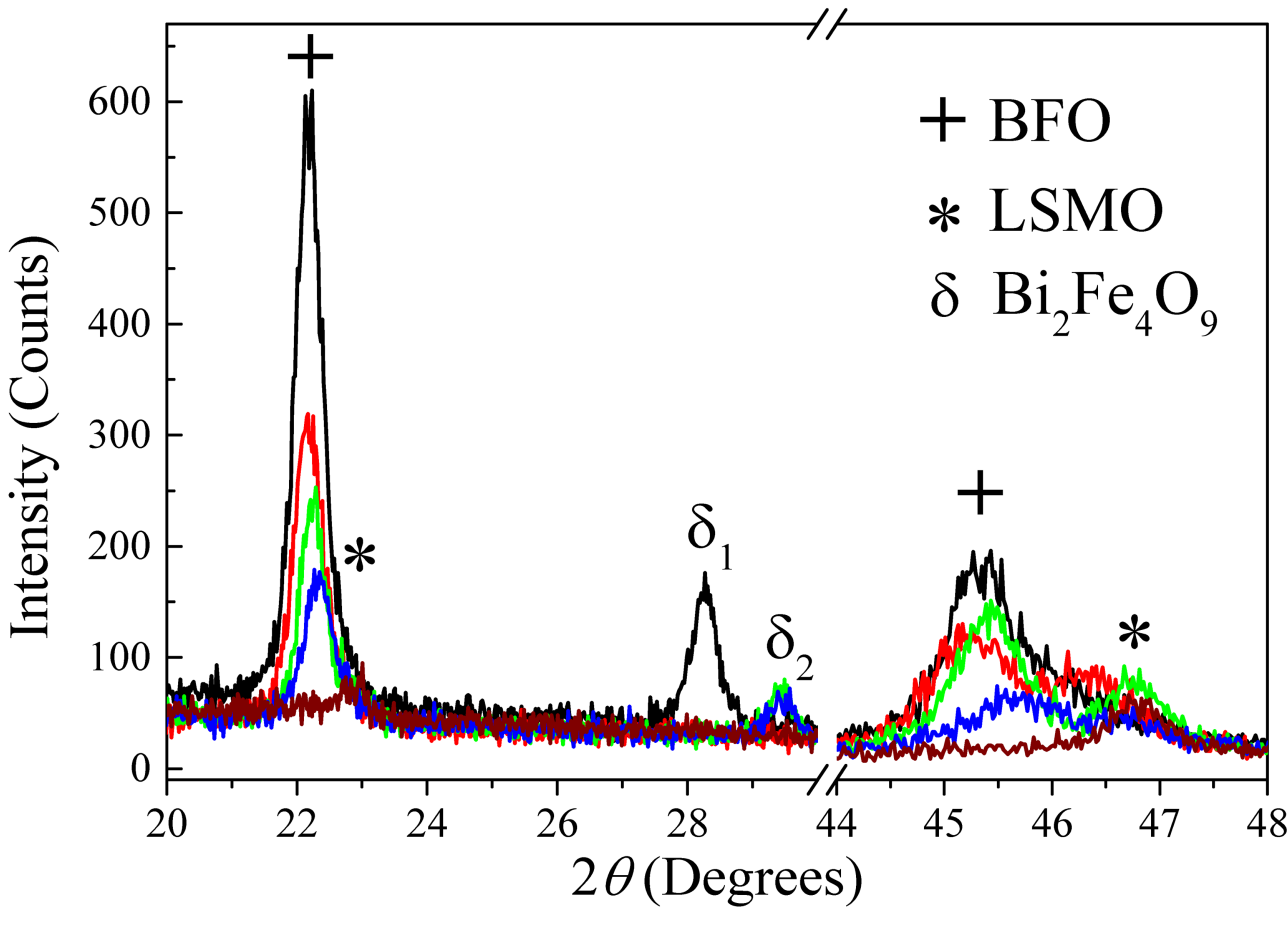
+ BFO
* LSMO
δ Bi2Fe4O9
δ1
δ2
Intensity (Counts)
0
100
200
300
400
500
600
20
22
24
26
28
44
45
46
47
48
2θ (Degrees)

(b)

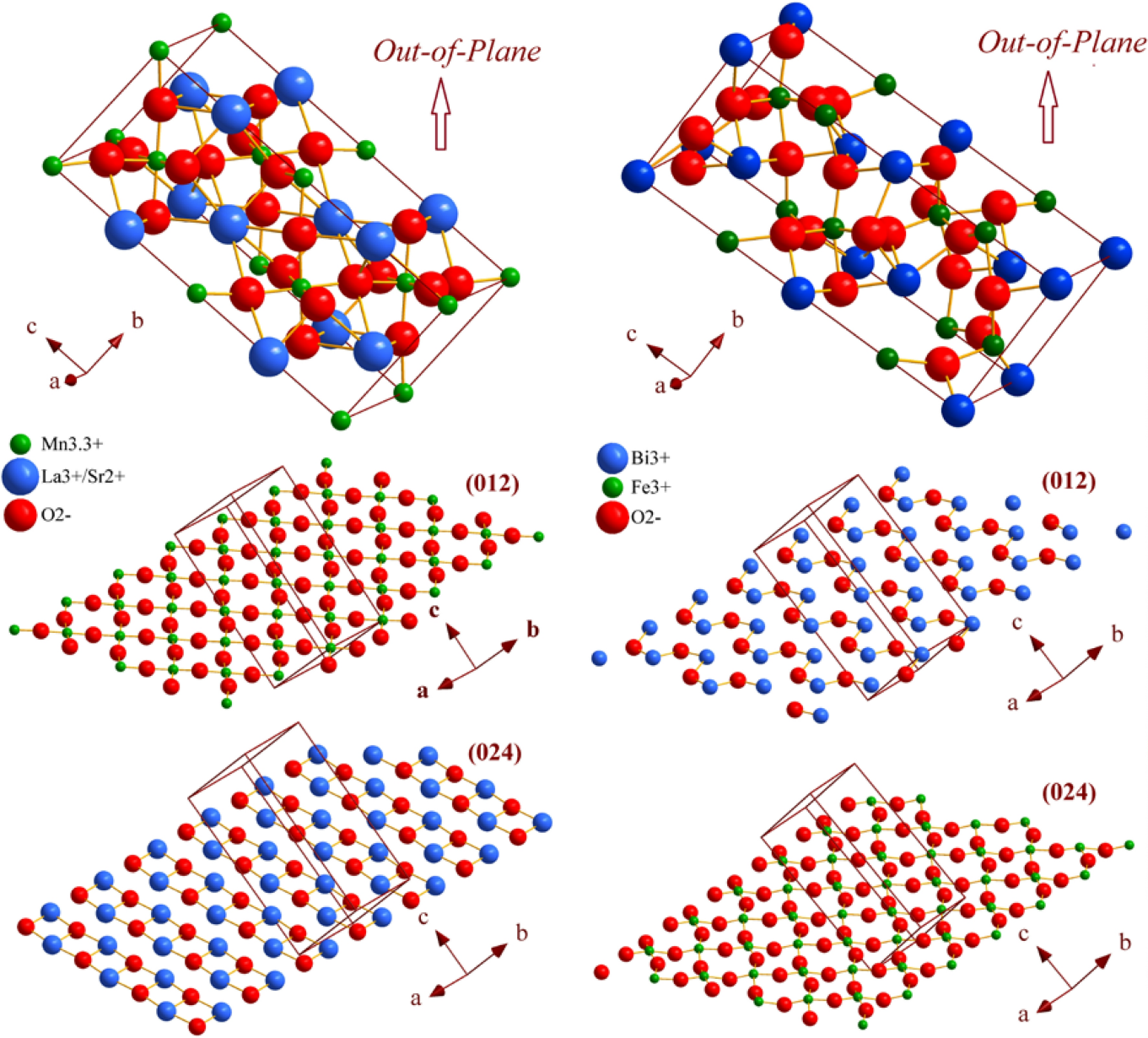
Out-of-Plane
c
b
a
Mn3.3+
La3+/Sr2+
O2-
(012)
(024)
Out-of-Plane
Bi3+
Fe3+
O2-
(012)
(024)

(a) (b)

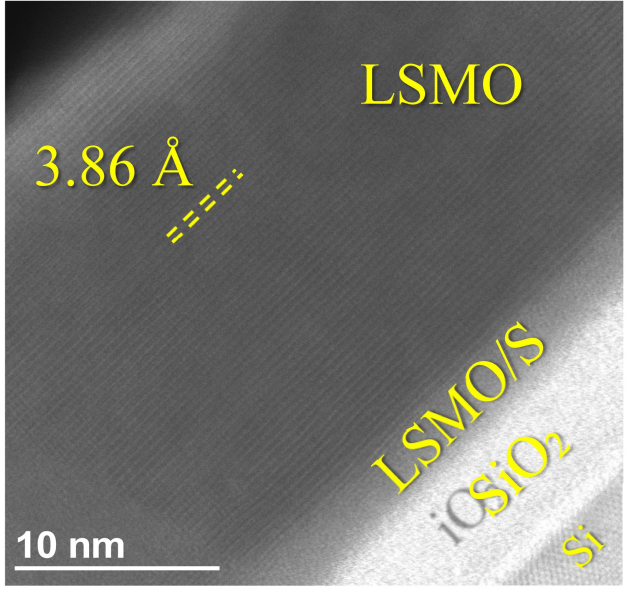
LSMO
3.86 Å
LSMO/S
iO2
Si
10 nm

(a)

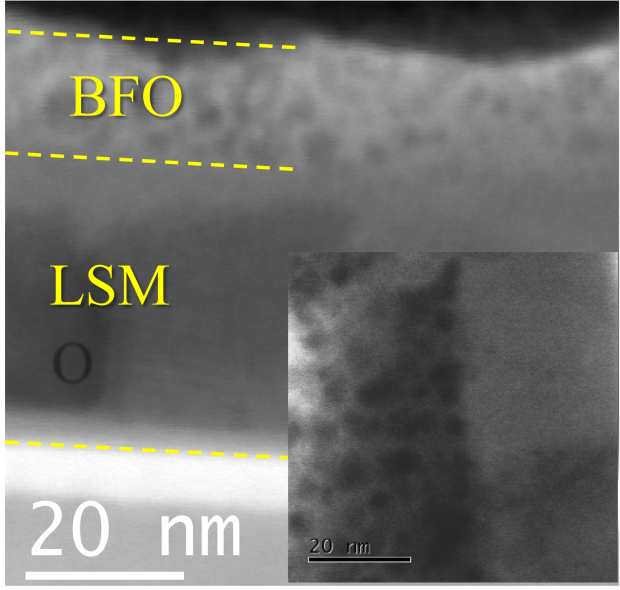
BFO
LSM
O
20 nm
20 nm

(b)

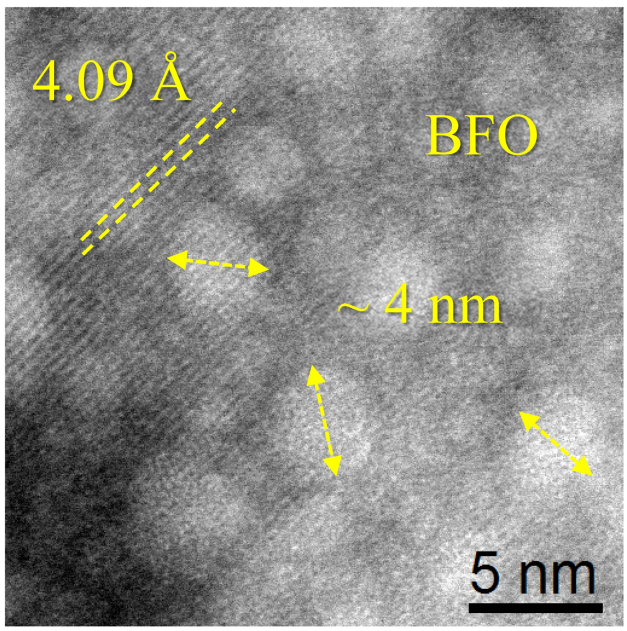
4.09 Å
BFO
~ 4 nm
5 nm

(c)

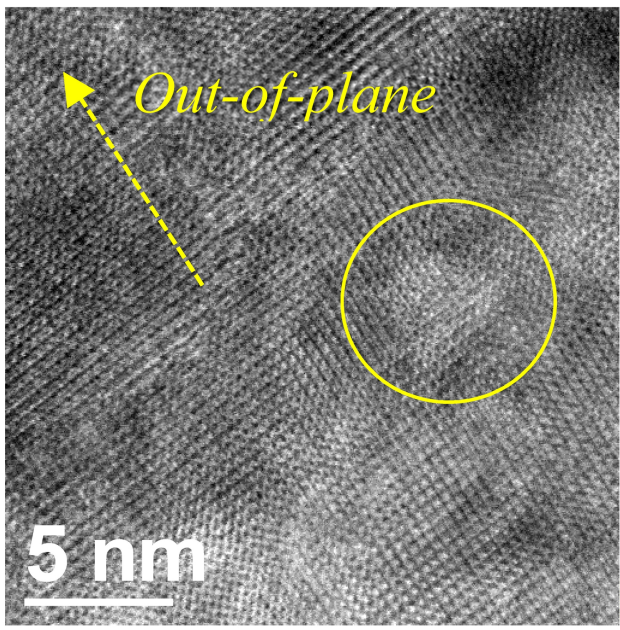
Out-of-plane
5 nm

(d)

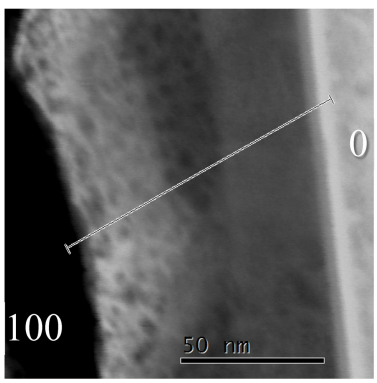
0
100
50 nm

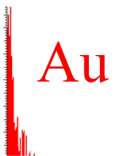
Au

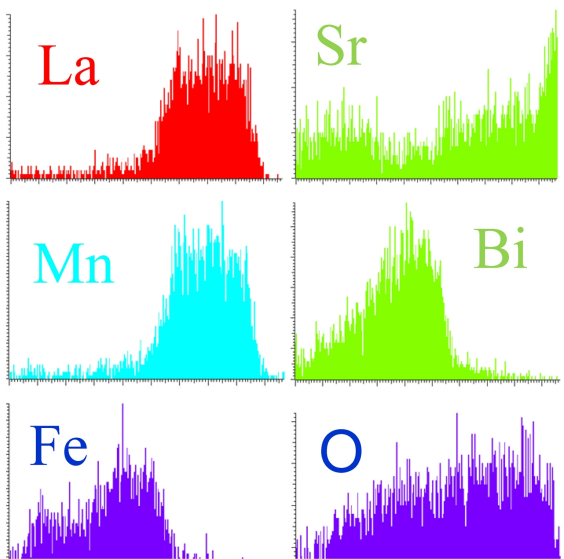
La
Sr
Mn
Bi
Fe
O

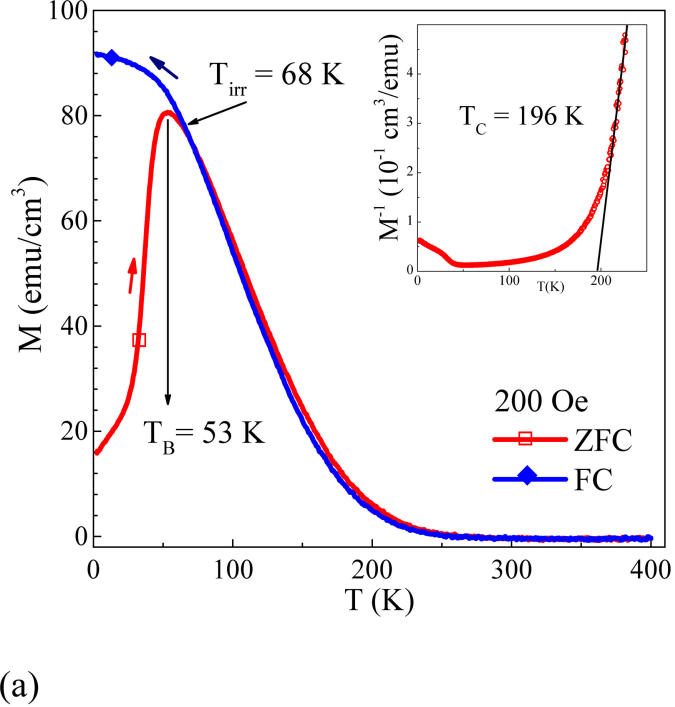
T_irr = 68 K
T_B = 53 K
T_C = 196 K
M^-1 (10^-1 cm^3/emu)
T(K)
200 Oe
ZFC
FC
M (emu/cm^3)
T (K)

(a)

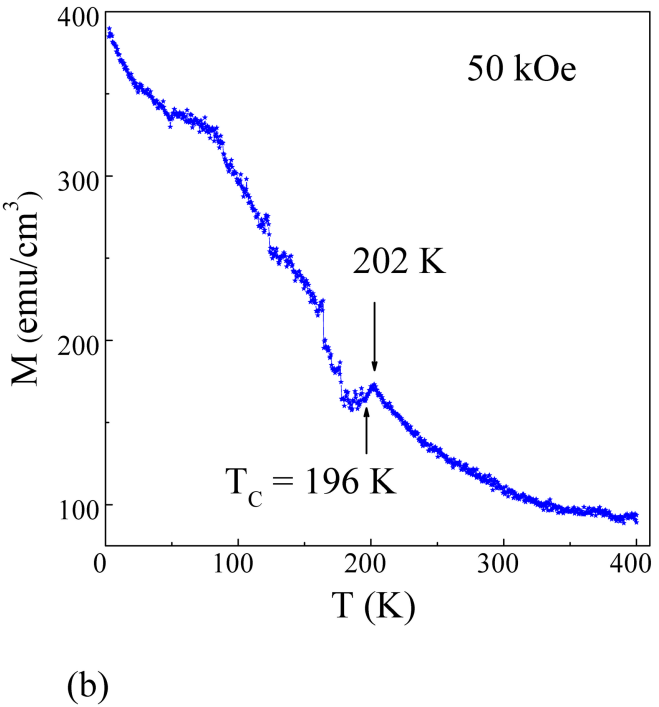
50 kOe
202 K
T_C = 196 K
M (emu/cm^3)
T (K)

(b)

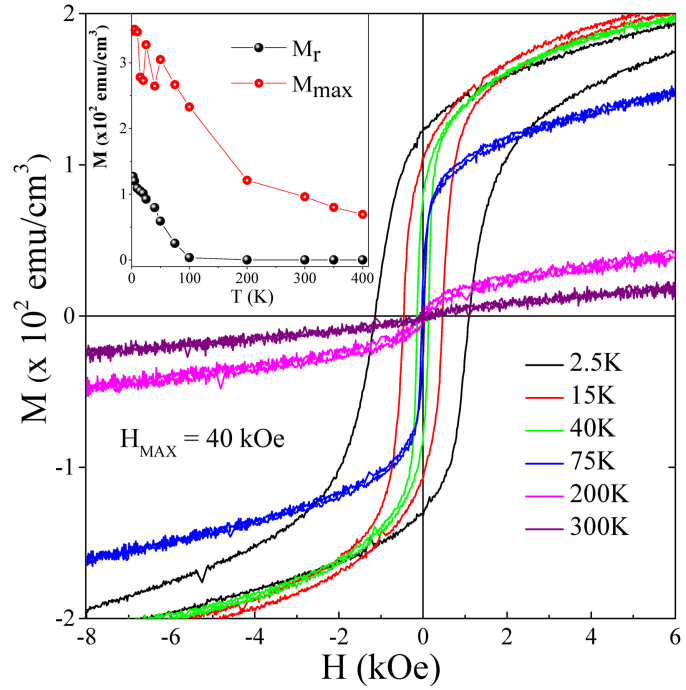
M_r
M_max
M (x10^2 emu/cm^3)
T (K)
H_MAX = 40 kOe
2.5K
15K
40K
75K
200K
300K
M (x 10^2 emu/cm^3)
H (kOe)

(c)

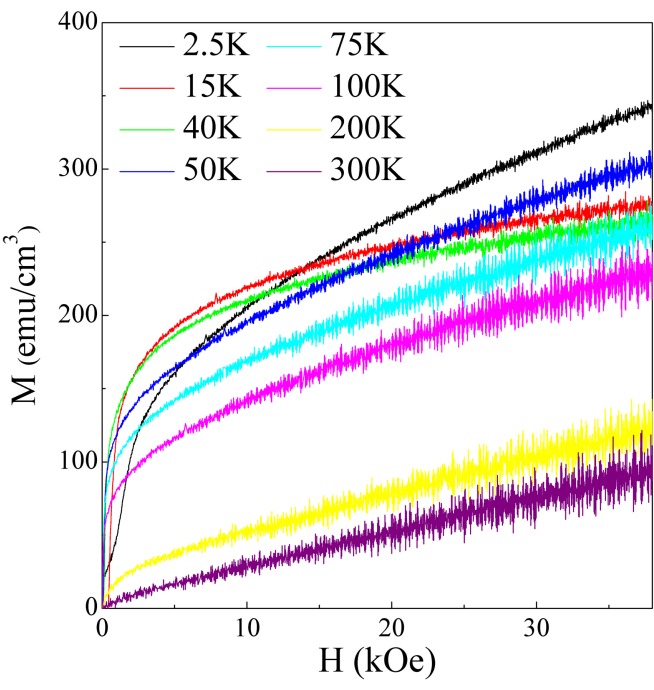
2.5K
15K
40K
50K
75K
100K
200K
300K
M (emu/cm^3)
H (kOe)

(d)

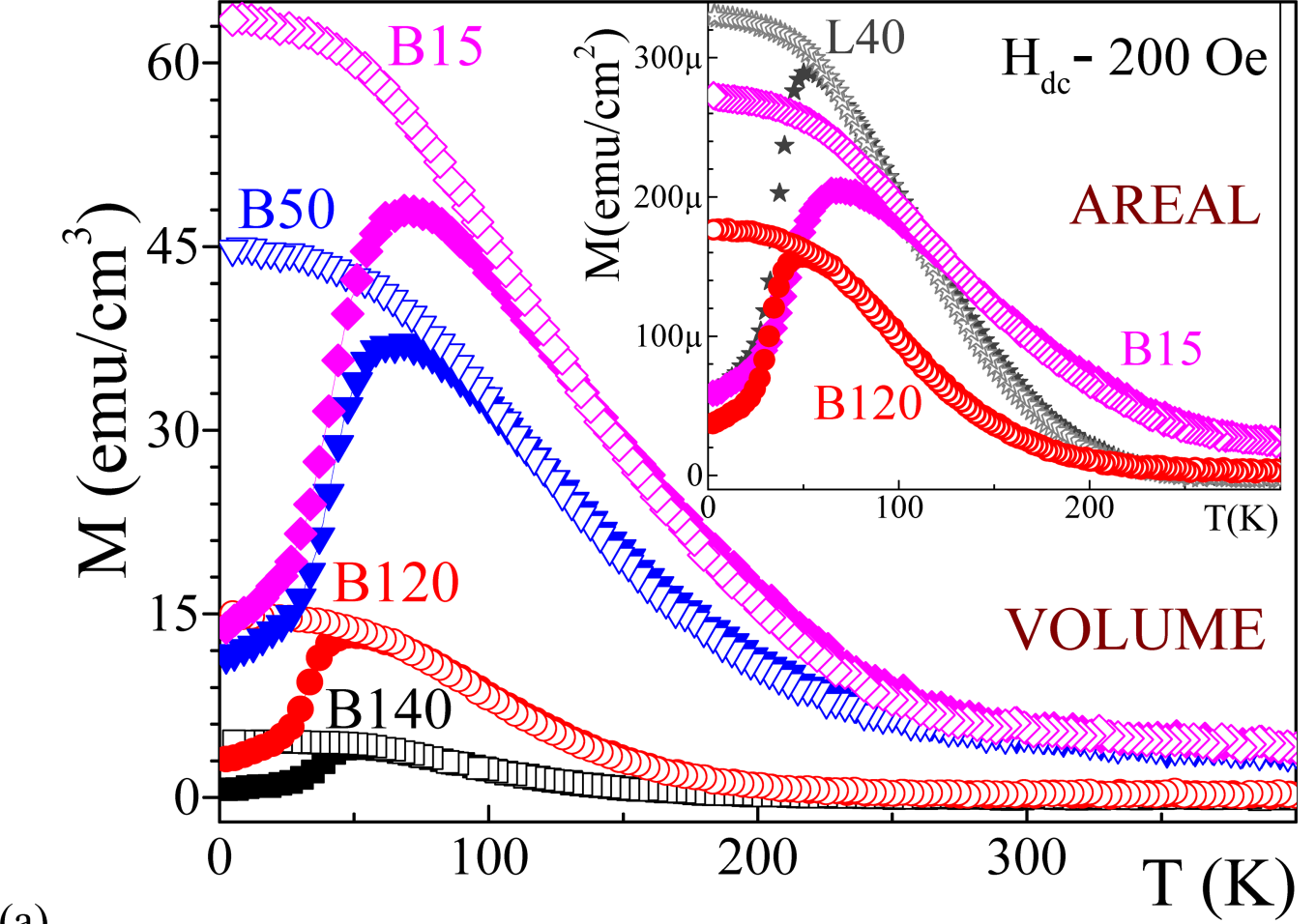
B15
B50
B120
B140
M (emu/cm^3)
T (K)
VOLUME
L40
H_{dc} - 200 Oe
M(emu/cm^2)
AREAL
B15
B120
T(K)

(a)

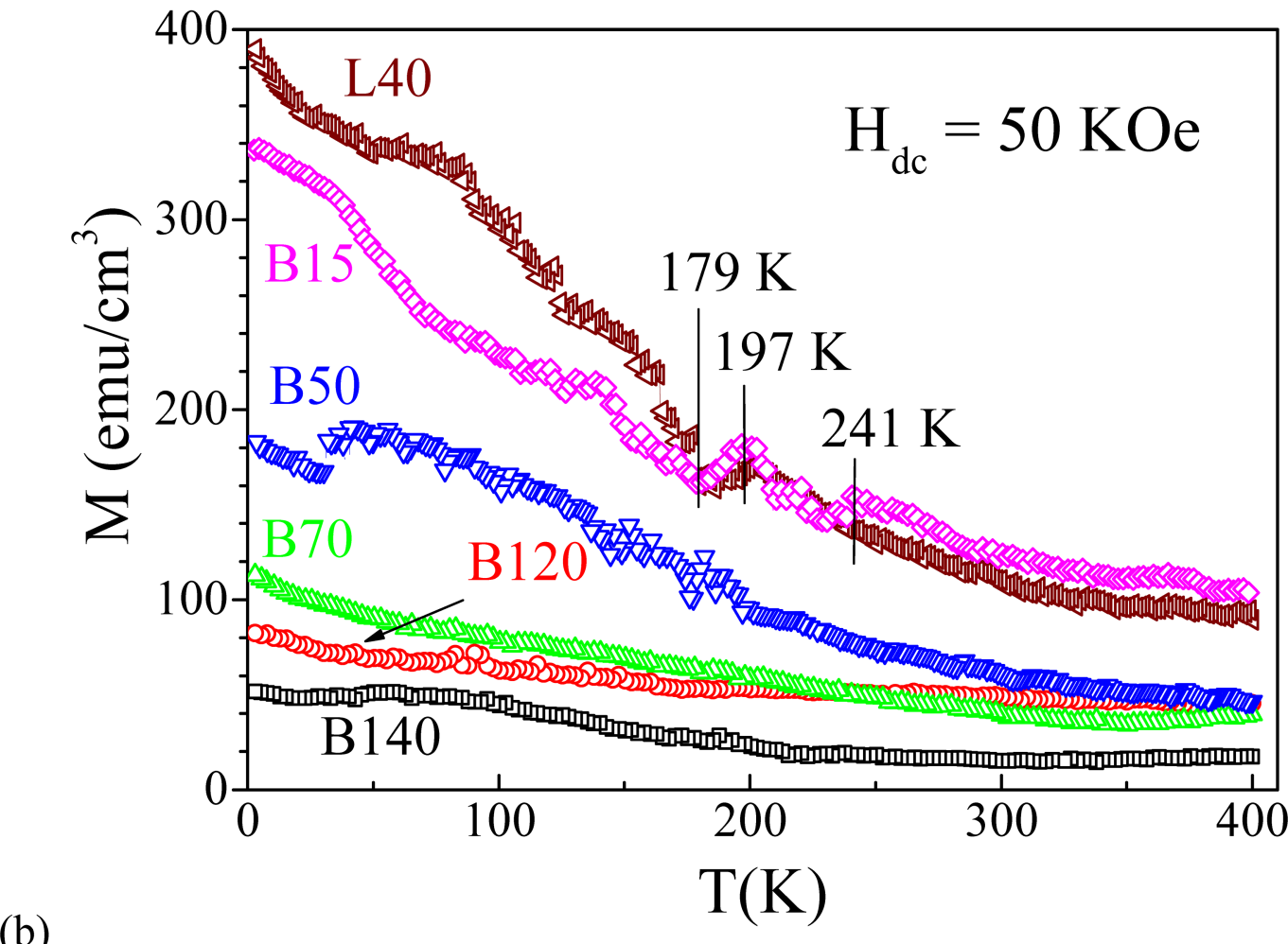
L40
H_{dc} = 50 KOe
B15
179 K
197 K
241 K
B50
B70
B120
B140
M (emu/cm^3)
T(K)

(b)

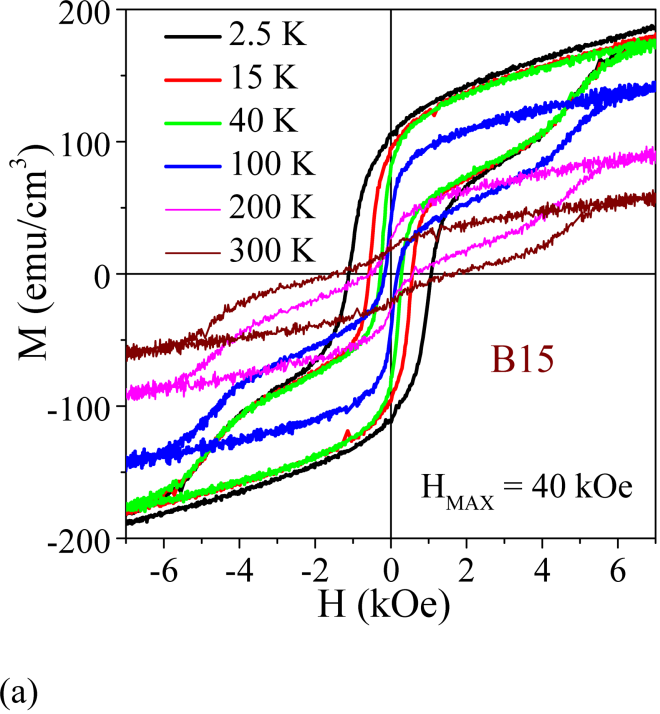
2.5 K
15 K
40 K
100 K
200 K
300 K
B15
H_MAX = 40 kOe
M (emu/cm^3)
H (kOe)

(a)

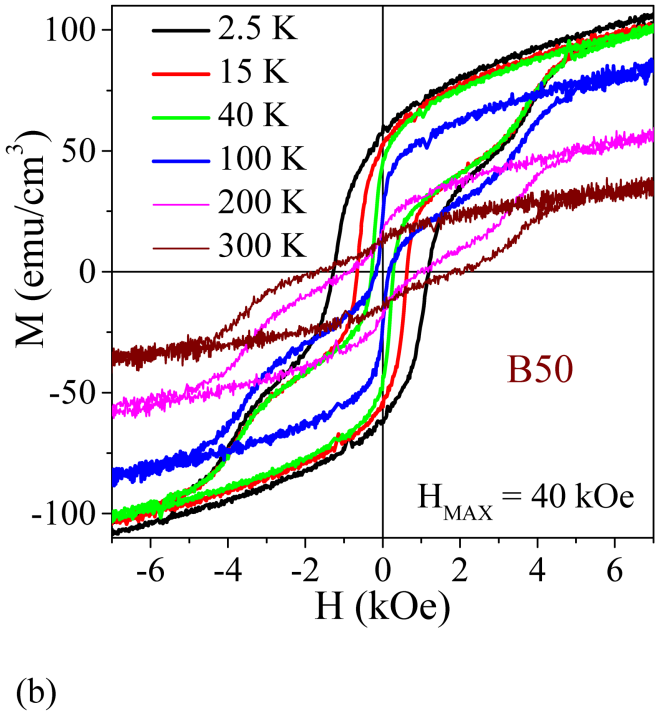
2.5 K
15 K
40 K
100 K
200 K
300 K
B50
H_MAX = 40 kOe
M (emu/cm^3)
H (kOe)

(b)

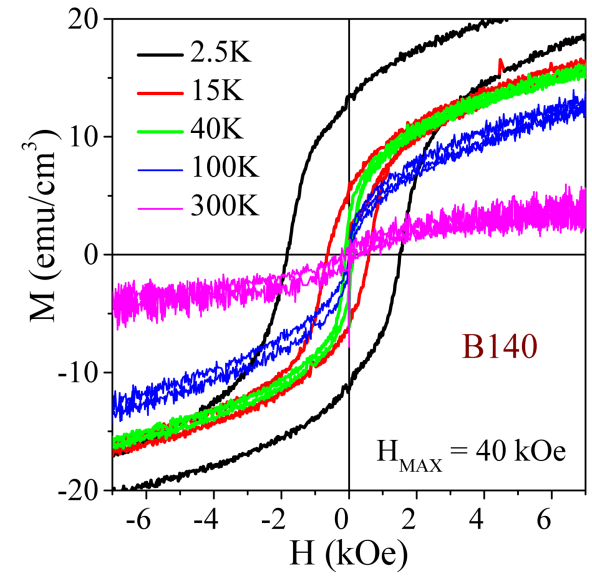
2.5K
15K
40K
100K
300K
B140
H_MAX = 40 kOe
M (emu/cm^3)
H (kOe)

(c)

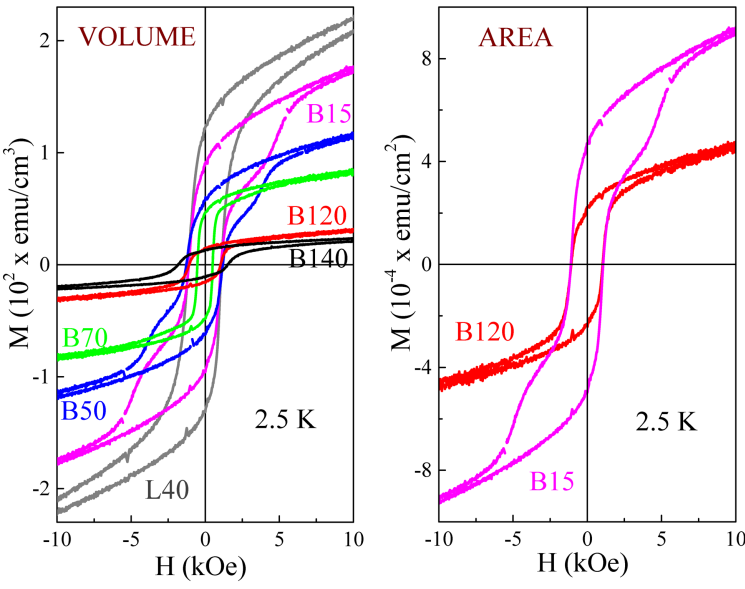
VOLUME
B15
B120
B140
B70
B50
L40
2.5 K
M (10^2 x emu/cm^3)
H (kOe)
AREA
B120
B15
2.5 K
M (10^-4 x emu/cm^2)
H (kOe)

(d)

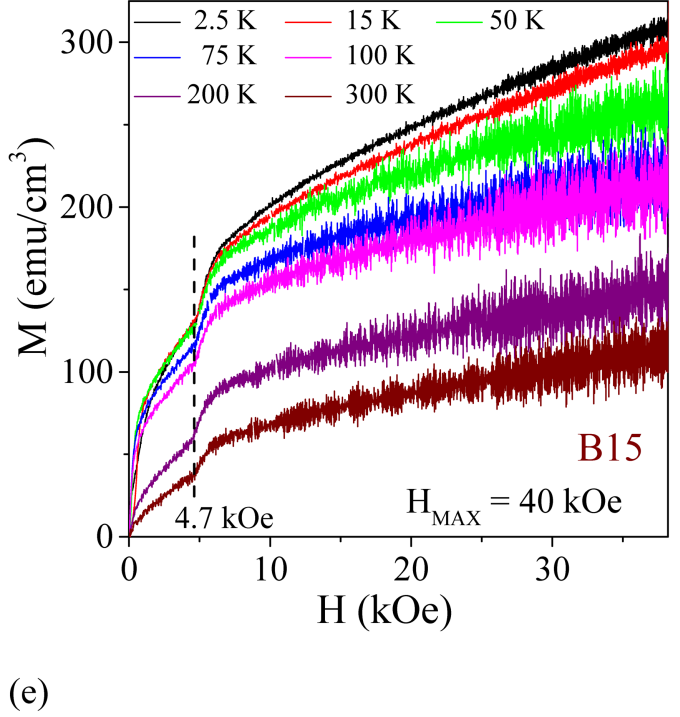

(e)

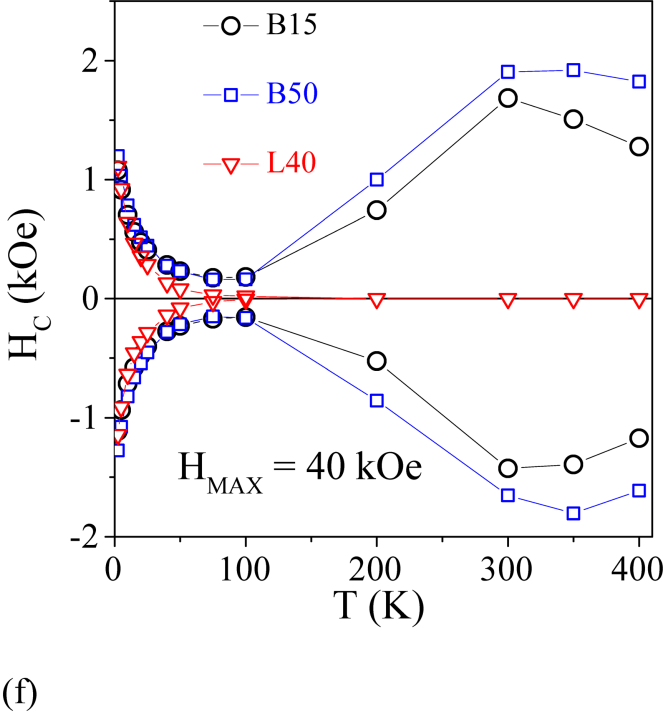

(f)

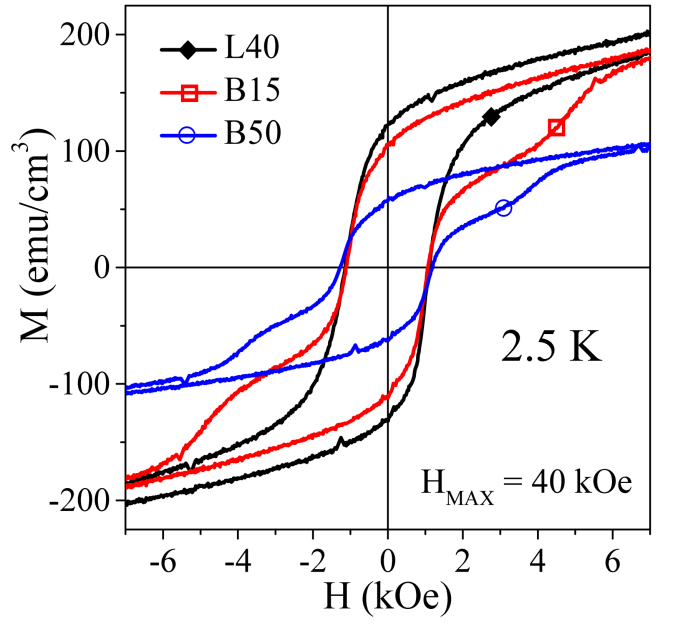

(g)

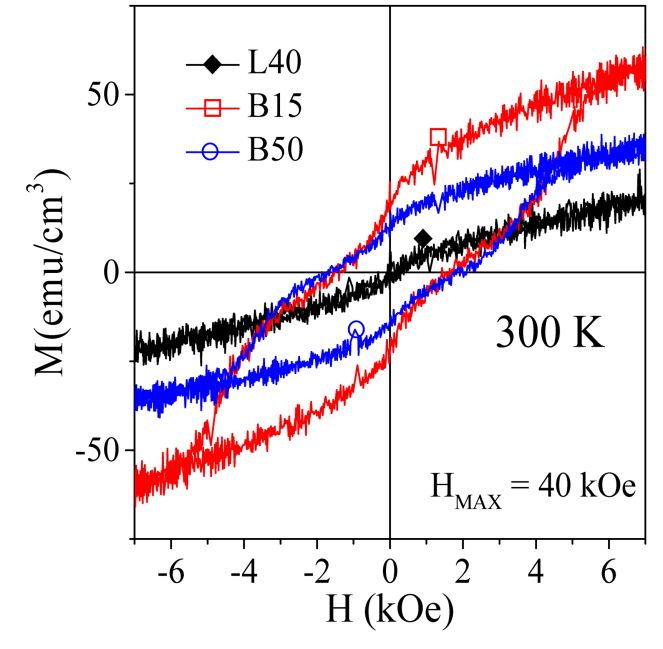

(h)

Figure 6. (Cont.)

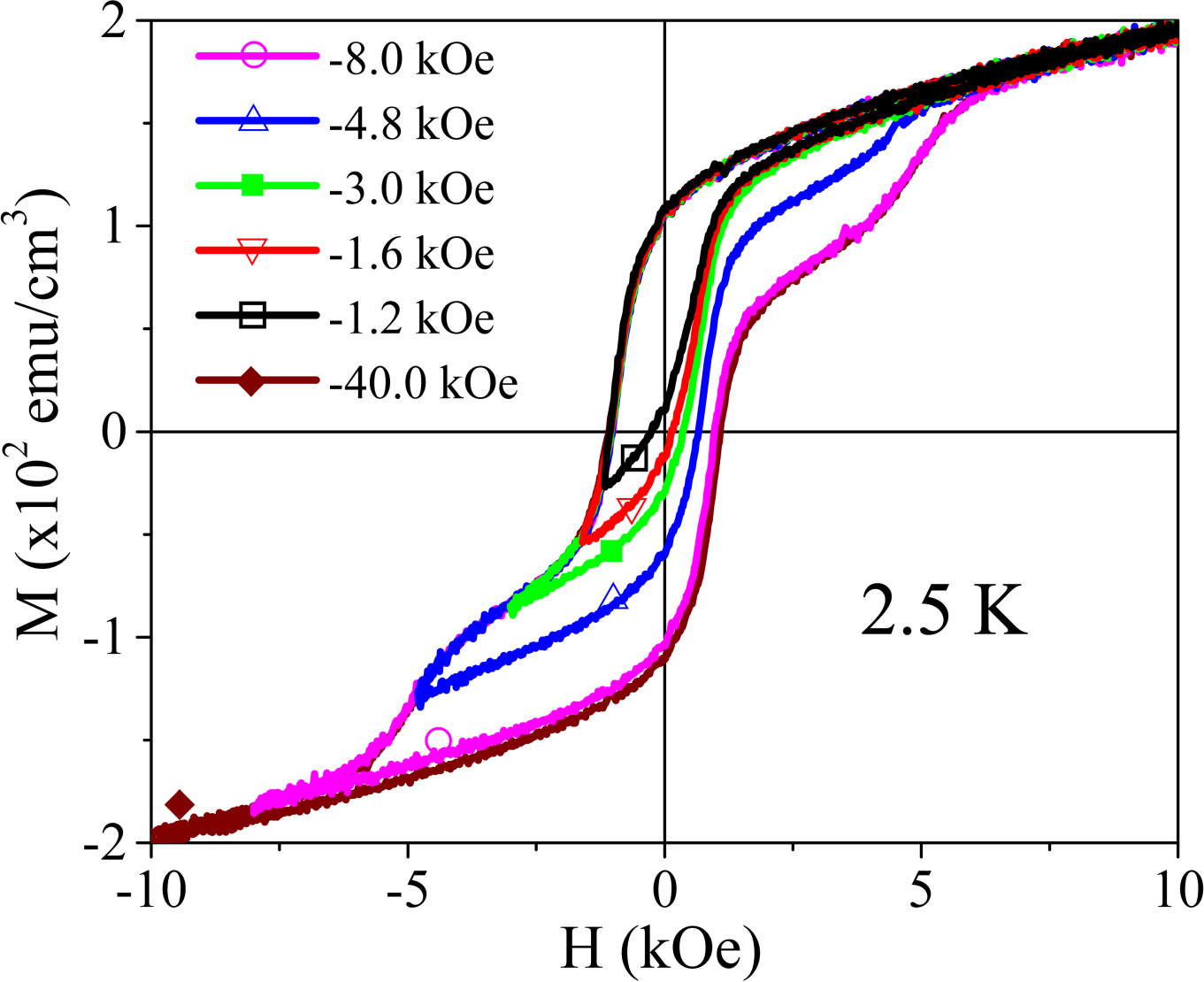
-8.0 kOe
-4.8 kOe
-3.0 kOe
-1.6 kOe
-1.2 kOe
-40.0 kOe
2.5 K
M (x10^2 emu/cm^3)
H (kOe)
2
1
0
-1
-2
-10
-5
0
5
10

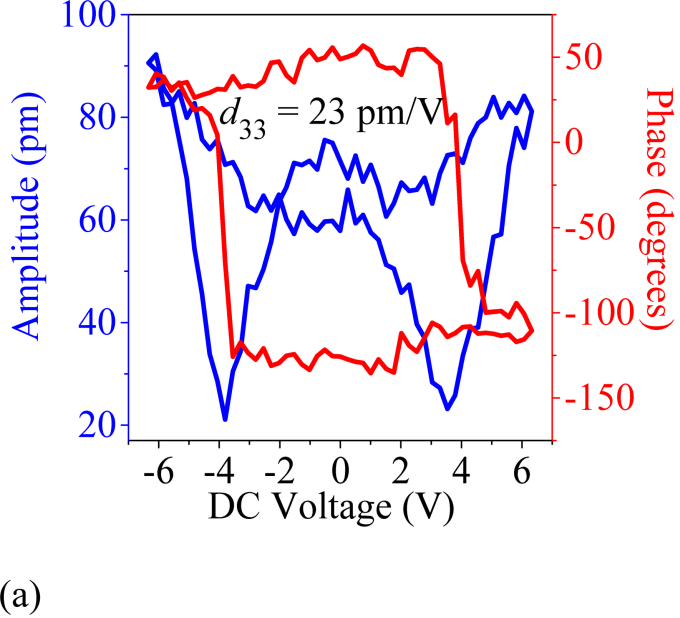
Amplitude (pm)
Phase (degrees)
d_{33} = 23 pm/V
DC Voltage (V)

(a)

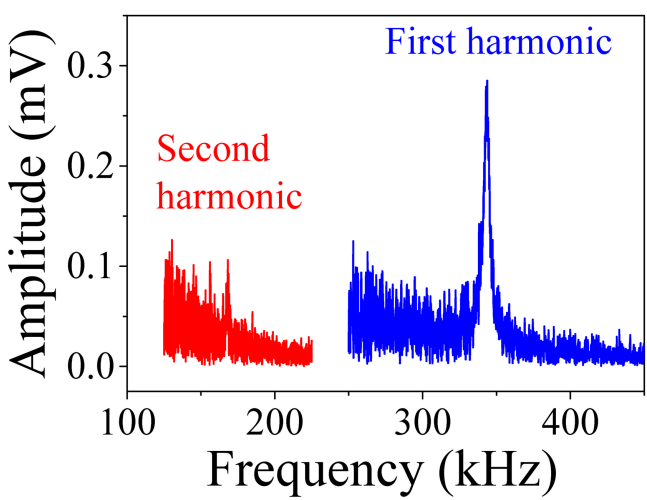
First harmonic
Second harmonic
Amplitude (mV)
Frequency (kHz)

(b)

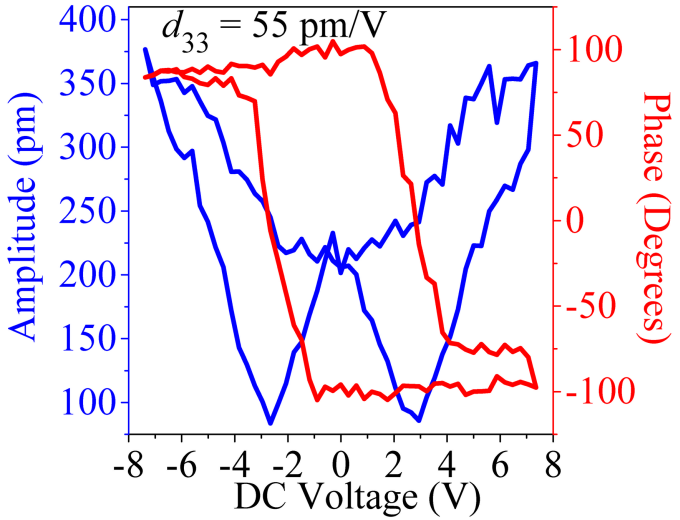
d_{33} = 55 pm/V
Amplitude (pm)
Phase (Degrees)
DC Voltage (V)

(c)

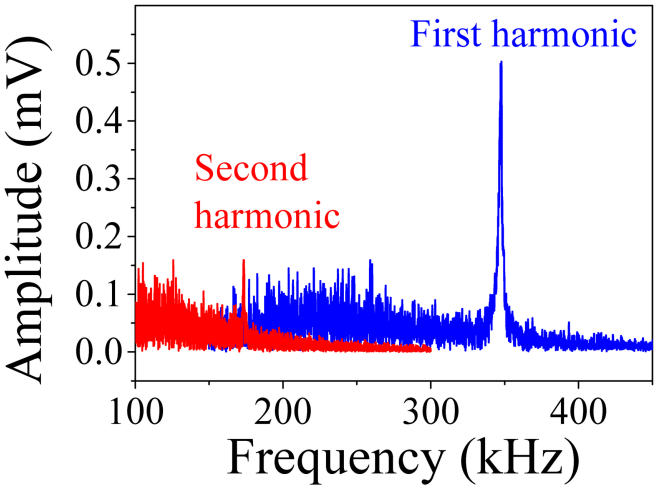
First harmonic
Second harmonic
Amplitude (mV)
Frequency (kHz)

(d)

$BiFeO_3$

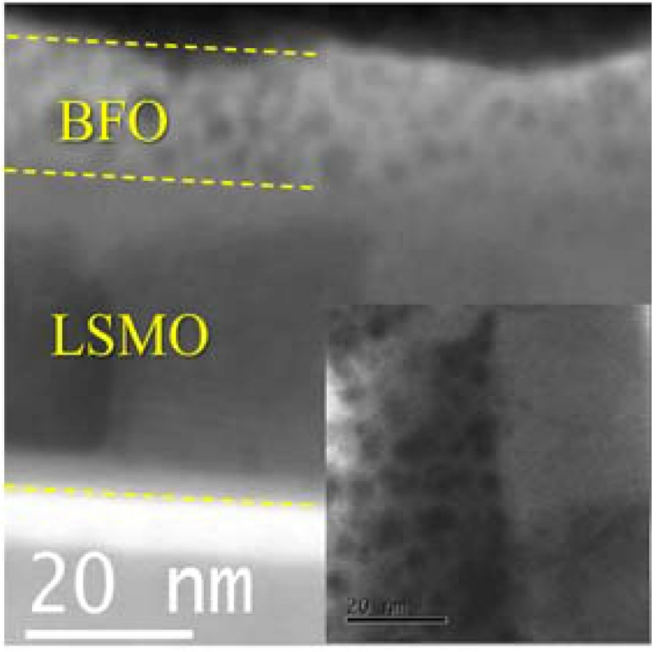

Ferromagnetic

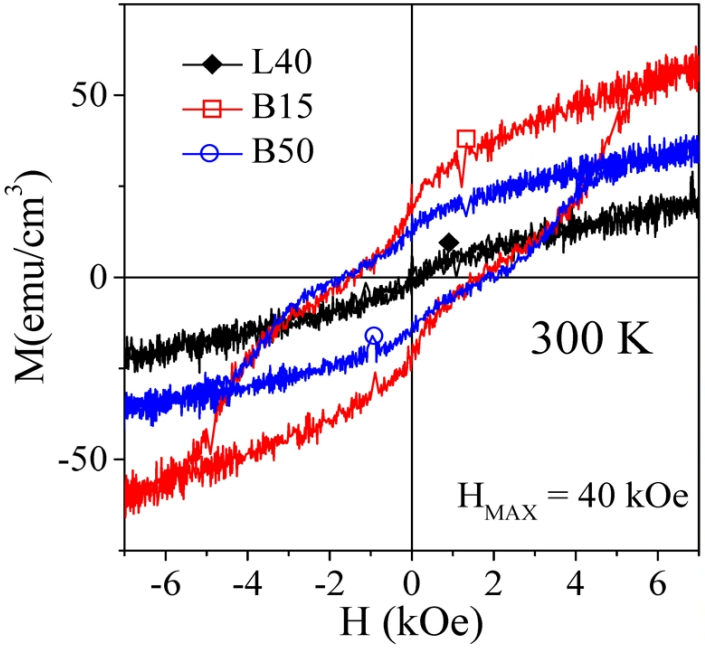

Ferroelectric